Fusion Engineering and Design 160 (2020) 111834

Contents lists available at ScienceDirect

Fusion Engineering and Design

journal homepage: www.elsevier.com/locate/fusengdes

3D modelling of MHD mixed convection flow in a vertical duct with transverse magnetic field and volumetric or surface heating

Tyler J. Rhodes*, Gautam Pulugundla, Sergey Smolentsev, Mohamed Abdou

UCLA, MAE Department, 44114 Engineering IV, 420 Westwood Plaza, Los Angeles, CA, 90095-1597, USA

ARTICLE INFO

Keywords:
Fusion
MHD
Mixed convection
Buoyancy
CFD

ABSTRACT

Understanding phenomena associated with the multiple effects/interactions of the fusion nuclear environment on liquid metal flow is required to correctly design liquid metal (LM) blankets for fusion facilities. These effects are investigated in the present work by numerically simulating 3D LM MHD flow. The simulated geometry consists of a straight, vertical duct which runs perpendicular to a strong, fringing applied magnetic field. There is also a region of applied heating as the primary goal is to explore buoyancy effects in MHD duct flows. Results are presented for both buoyancy assisted (upwards) and buoyancy opposed (downwards) flows in conducting and insulating ducts for a range of Hartmann numbers (*Ha*) up to 100, Reynolds numbers (*Re*) from 10^3 to 10^4 and Grashof (*Gr*) numbers from 10^7 to 10^8. While increasing *Gr* or decreasing *Re* increases buoyancy effects, increasing *Ha* was shown to increase maximum temperature through turbulence reduction. The extent to which the MHD mixed convection flows are quasi-2D is analyzed and buoyant effects, in competition with electromagnetic forces, are shown to bring about 3D flow features not seen in purely MHD flows. Volumetric nuclear heating with steep gradients is applied to the vertical MHD flows for comparison to flows with surface heating only. Surface heating generates stronger buoyancy effects than volumetric heating of the same total power; however, many of the same phenomena occur. Therefore, surface heating, the only option for lab experiments, can provide indication of the effects of volumetric heating in MHD flows.

1. Introduction

The volumetric nuclear heating induced by neutrons and secondary gamma rays in liquid metal (LM) fusion blankets has steep gradients along the radial direction with the majority of the heating occurring near the first wall [1]. The heating decreases rapidly moving outwards along the radius of the reactor as the neutron flux is attenuated by the LM. Such high radial gradient in heating is bound to produce temperature gradients which will in turn give rise to buoyant forces. Buoyant force is oriented opposite to the direction of gravity and the orientation of the LM blanket flows will vary along the perimeter of the reactor's core [2], so the possible buoyant effects have a wide spectrum of phenomena with many important configurations to study. Moreover, there is the simultaneous effect of the strong magnetic field to consider, the strength of which also varies by location inside the reactor. Depending on the flowrate, magnetic field, and relative strength of buoyant effects, the flow regime may be that of MHD forced flow, weakly unsteady MHD mixed convection, or strongly unsteady MHD mixed convection where turbulence is expected to appear in a special form of quasi-two-dimensional (Q2D) turbulence. Such flows are characterized by Hartmann (*Ha)*, Reynolds (*Re)*, and Grashof numbers (*Gr),* which are defined in section 2.

While many studies have been performed for MHD duct flows in the context of fusion research and development, relatively few studies have included the combined effect of buoyancy and MHD simultaneously in 3D as in the present work.

Buoyancy driven MHD flows have been investigated in many studies. Bühler (1998) [3] performed asymptotic analysis on flow in long vertical ducts with transverse magnetic fields and various heating modes. His analysis, which assumes $Ha^4 >> Gr$, suggests the inviscid core does not necessarily behave two-dimensionally and that large jets attached to the sidewalls will carry most of the flow for conducting walls. The problem was revisited by Mistrangelo and Bühler (2011) [4] using numerical methods, confirming the previous conclusions and validating their numerical approach.

Zikanov et al. (1998) [5] performed DNS type simulation of a vertical duct flow with periodic axial boundaries driven by uniform axial temperature gradients. The focus of their study was on elevator modes: antiparallel vertical jets which grow due to buoyant effect. They found the elevator modes to be stabilized by an axial applied magnetic field to

* Corresponding author.
E-mail address: tjrhodes@ucla.edu (T.J. Rhodes).

https://doi.org/10.1016/j.fusengdes.2020.111834
Received 5 August 2019; Received in revised form 27 May 2020; Accepted 13 June 2020

enhance vertical heat transfer.

There have been experimental efforts to study MHD mixed convection duct flows. Experiments in Russia by Melnikov et al. (2013) [6] as part of the MPEI – JIHT RAS MHD-facility showed significant low frequency, high magnitude, temperature fluctuations in downward flow of mercury in a round tube heated on one side via radiation. Experiment on a rectangular duct in the same facility by Kirillov et al. (2016) [7] also showed periodic temperature fluctuations but also included velocity data which indicated significant asymmetry due to buoyant effects in downward MHD flow of mercury. Belyaev et al. (2018) [8] studied MHD mixed convection in a vertical pipe with transverse magnetic field and uniform surface heating using the more recent HELM Experimental Facility at the JIHT RAS. The experimental results indicated that the magnetic field promoted high amplitude temperature fluctuations at moderate *Ha* (300-350) but suppressed fluctuations at higher *Ha* (>500) for *Re* on the order of 10^4 and *Gr* on the order 10^7. The present work provides numerical results for future comparisons of this experiment which consists of vertically driven PbLi in a square duct with one-sided surface heating and a region of uniform, transverse magnetic field.

In the past few decades, there have been substantial numerical efforts to explore the combined effects of MHD and buoyancy in vertical MHD mixed convection duct flows with transverse magnetic fields and applied heating. However, in order to reduce the cost of computations, researchers mostly limited their investigations to 2D flows, either by studying the fully developed flow, or by assuming the flow is quasi-2D. The former assumes that the velocity does not change along the flow direction while the latter assumes that the velocity does not change along the magnetic field direction (outside of the boundary layers).

Fully developed downward flows in vertical ducts with both MHD and buoyancy were studied by several researchers. Smolentsev et al. (2008) [9] found analytical solutions of fully developed flows in insulated vertical ducts with exponential volumetric heating and transverse magnetic field and performed numerical computations using a Q2D approach. The results of the two approaches showed good agreement and indicated the occurrence of flow reversal in buoyancy opposed MHD flows for the first time. The flow reversal was also characterized by the steepness of the heating curve and a ratio of the parameters *Ha*, *Re*, and *Gr*. Based on Smolentsev's prediction of flow reversal in buoyancy opposed MHD flows, blanket designs are recommended to avoid having downward flows in channels closest to the first wall. Sposito and Ciofalo (2008) [10] published an analytic temperature solution and numerical velocity and electric potential solutions for vertical square ducts with variable wall conductivity and applied magnetic field and uniform volumetric heating. Saleh and Hashim (2010) [11] studied fully developed downward flow in insulating ducts numerically. Mistrangelo and Bühler (2012) [12] numerically investigated the effects of changing the transverse magnetic field direction relative to the applied surface heating and changing the electrical conductivity of the walls by considering fully developed flows. Chutia and Deka (2012) [13] studied fully developed flow using MATLAB with low parameters *Gr, Ha* $\sim 10^2$ and $Re = 1$. Zhang and Zikannov [14] used a Q2D model to study turbulent convection in horizontal pipes in 2015. Later, in 2018 [15] they studied instability and flow reversal in vertical MHD flows with applied heating and a transverse magnetic field. All studies featuring downward flows with strong buoyancy effects reported considerable flow reversal.

Liu and Zikanov (2015) [16] numerically simulated vertical MHD mixed convection duct flow with a transverse magnetic field and a heated wall using a quasi-2D formulation to observe stable elevator modes.

Various studies of mixed convection MHD flows focusing on Q2D MHD turbulence and laminar-turbulence transition in conditions relevant to the Dual Coolant Lead Lithium (DCLL) blanket, including radially decaying volumetric heating, were performed by a group of UCLA researchers led by S. Smolentsev. The main results of these studies have been summarized in Refs. [17] and [18]. Efforts have been made to model 3D mixed convection flow phenomena in fusion blanket relevant conditions for buoyancy assisted (upward) and buoyancy opposed (downward) flows. The studies included linear stability analysis and DNS-type computations for MHD inflectional instabilities for MHD mixed convection upward flows with volumetric heating using the Q2D flow model for various *Gr* up to 10^9, *Re* up to 10^4 and *Ha* up to 500. Steady, weak turbulence, and strong turbulence regimes were characterized based on the dimensionless parameters. Lastly, fully 3D numerical modeling using HIMAG was performed for the sake of comparison with buoyancy assisted duct flow solutions from Q2D models and analytic solutions for fully developed flow [9].

Zikanov and Listartov (2016) [19] simulated the test section geometry of Melnikov et al. (2013) [6] which included a vertical pipe flow with transverse magnetic field and onesided heating. From the results, they identified the mechanism behind temperature fluctuations observed in experiment and they explain the mechanism as "the growth and breakdown of elevator convection modes". Listratov et al. (2018) [20] simulated horizontal pipe flow with a transverse magnetic field and one-sided uniform heating from below to study the effect of *Ha*, *Re*, and *Gr* on high amplitude temperature fluctuations from buoyant effects.

The studies on the combined effects of MHD and buoyancy in the present work reveal new phenomena which may influence many aspects of blanket design including thermomechanical fatigue and corrosion of the duct walls, tritium permeation, and heat transfer for power generation. Moreover, the results presented in this paper will be valuable for the development of future numerical tools and for comparison with new experimental results.

This paper is organized as follows: Section 2 contains a description of the problem formulation and numerical methods used; Section 3 contains a discussion of the physics and phenomena of MHD mixed convection flows, a parametric study of magneto-buoyant effects, an analysis of non-uniformity along the magnetic field direction, and a comparison of volumetric heating cases which approximate nuclear heating to surface heating cases; Section 4 contains a summary of conclusions.

2. Physical and mathematical models

To study MHD mixed convection flow behavior, a 3D MHD solver HIMAG [21] was used to simulate the flow of liquid metal through a vertical, straight, square duct subject to applied onesided heating and a fringing, transverse magnetic field (Fig. 1). The origin for the coordinate system is at the center of the duct's cross-section in the center of the heated region. Uniform flow enters the duct in a zero-magnetic field region. The flow continues into a region with a fringing, y-direction magnetic field which is uniform for 80 cm along the duct. Inside the uniform magnetic field region, the flow encounters a 60 cm region where heating is applied either as volumetric heating in the fluid or as surface heating on the $z = -a - t_w$ sidewall, where t_w is the wall thickness. The flow exits the duct, fully developed, through a region of zero-magnetic field. The final 40 cm of the duct has artificially high viscosity for numerical reasons.

Such a flow is characterized by the following key dimensionless parameters: the Hartmann number, which when squared, represents the strength of electromagnetic forces relative to viscous forces, $Ha = bB_o\sqrt{\sigma/\nu\rho}$, where *b* is the halfwidth of the duct along the magnetic field direction, B_o is the maximum applied magnetic field strength, σ is the electrical conductivity, ν is the kinematic viscosity, and ρ is the fluid density; the Reynolds number, which represents the strength of inertial forces relative to viscous forces, $Re = \frac{aU}{\nu}$, where a is the duct half width perpendicular to the magnetic field and *U* is the mean velocity; the Grashof number, which represents the strength of buoyant force relative to viscous force, $Gr = \frac{g\beta\Delta Ta^3}{\nu^2}$, where *g* is the magnitude of

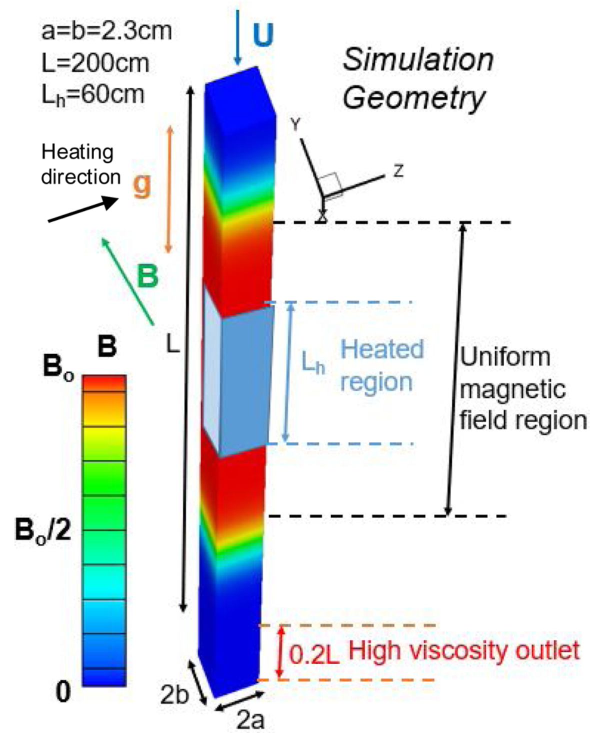

Fig. 1. A test blanket submodule geometry for numerical simulation.

acceleration due to gravity, β is the coefficient of thermal expansion, and ΔT is a characteristic temperature difference; the wall conductance ratio, $c_w = \frac{\sigma_w t_w}{\sigma b}$, where σ_w is the electrical conductivity of the walls; and the Prandtl number, which is the ratio of viscous diffusion to thermal diffusion, $Pr = \frac{\rho \nu C_p}{k}$, where C_p is the specific heat capacity of the fluid and k is the thermal conductivity of the fluid. In the definition of Gr, ΔT is a characteristic temperature difference calculated using the following formula:

$$\Delta T = \frac{a}{k}\int_{-a}^{+a} q'''(z)dz \tag{1a}$$

for volumetric heating,

$$\Delta T = \frac{a}{k} q_o'' \tag{1b}$$

for surface heating.

In Eq. (1a), $q'''(z)$ is the distribution of applied heating per unit volume inside the fluid domain. In Eq. (1b), q_o'' is the prescribed heating per unit area in the special case that the heating mode is purely surface heating applied to the outside surface of the sidewall. The axial length of the heated region, L_h, in all cases is 0.6096 m centered at x = 0 m. In the volumetric heating ca ses, the heating spans the fluid domain uniformly from y = -b to y = b and is largest at the z = -a sidewall and decreases exponentially or otherwise follows the trend of nuclear heating data towards the z = a sidewall. In surface heating cases, the heating is uniform at z = -a-t_w, spanning from y = -b-t_w to y = $b + t_w$.

The total axial length is 2.4 m which is close to the poloidal blanket length in some design studies [22]. The final 0.4 m are included for numerical reasons discussed later in this section. The duct has a square cross section such that $a = b$ = 0.023 m. Physical properties of the LM were chosen to equal those of eutectic lead-lithium alloy (PbLi) at 300 °C (Pr = 0.033) while the physical properties of the wall were chosen to be those of stainless steel at 300 °C (c_w = 0.12) or those of an insulating wall ($c_w = 1.2 \times 10^{-9}$).

The simulated magnetic field fringes to imitate the field of an electromagnet which produces a region of uniform field with an axial length of 0.8 m centered at x = 0 m. The shape of the field is defined in the following way. Firstly, the domain is divided into three types of regions: 1) a downstream region where the magnetic field is zero, 2) a uniform region, and 3) two fringing regions which boarder the uniform region:

1) If $x \geq x_o + 2^*(x_c - x_o)$ then $B = 0$. (2a)

2) Else if $x_1 < x < x_2$ then $B = B_0$. (2b)

3) Else if $x_1 > x$ or $x > x_2$ then B=

$$\frac{1}{2}B_0{}^*\left(1 - 0.1^*\tanh\left(\frac{|x - x_c|}{c_1} - c_2\right)\right) \tag{2c}$$

Here, $x_c = \frac{x_2 + x_1}{2}$ and x_1 and x_2 are the boundaries of the uniform field region. x_o is the location of the duct entrance. In the present cases, x_1 = -0.4 m and x_2 = 0.4 m and so x_c = 0 m. B_0 is the uniform magnetic field strength (e.g. 0.5 T). c_1 is set to 0.01 m in the simulations such that the argument inside the tanh function reads $(\frac{|x|}{0.01m} - c_2)$ and here, x ranges from -1 m to 1.4 m. c_2 is a constant equal to 73.15. The magnetic field distribution is uniform in y and z and its magnitude along the axial direction is plotted in Fig. 2.

The HIMAG code solves the MHD equations coupled with the thermal energy equation, shown below as Figs. 3–7, in 3D using an electric potential formulation with the assumption that the induced magnetic field is small enough to be neglected compared to the applied one (low magnetic Reynold's number approximation). Furthermore, the fluid is assumed Newtonian and incompressible, and Joule heating and heating from viscous dissipation are assumed negligible compared to the applied heating. Additionally, the Boussinesq approximation (BA) is applied such that all material properties are assumed constant except for the inside the buoyant force term of Eq. (4), where it is as though density decreases linearly with increasing temperature.

The BA is a powerful and convenient approach to making non-isothermal problems tractable for numerical investigation; however, the errors associated with using BA are difficult to quantify. Currently, no studies have analyzed the applicability of the BA in MHD flows despite the fact that use of BA is widespread for such problems (e.g. [4, 5, 12-19]). And though the only sure way to evaluate error related to BA in a particular flow is to compare with results of methods which do not employ BA, a preliminary justification for using BA can be made using some criteria developed for hydrodynamic flows.

Criteria for applicability of BA in hydrodynamic flows have been published [23–26], the simplest of these, put forth by Crapper and Bains (1977) [23], stipulates that the density should change by no more than 5% by thermal expansion. To achieve a 5% decrease in the density of PbLi, the temperature would need to exceed 713 °C [27], approximately 160 °C greater than the maximum temperature of the present simulations. Additional criteria, such as $\frac{\nu}{(gb)^{.5}b} \ll 1$ (presently $\sim 2 \times 10^{-5}$), $\frac{U}{(gb)^{.5}} \ll 1$ ($\sim 6 \times 10^{-2}$), and others which ensure incompressibility of the fluid and negligible heating from viscous dissipation [26], are also satisfied in the present simulations.

Therefore, our approach is to use the BA in the present work and to suggest that future efforts be made to rigorously qualify the use of BA

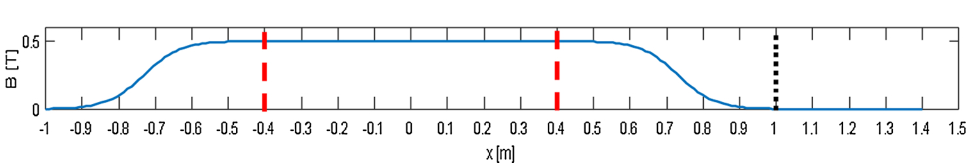

Fig. 2. An example magnetic field plotted using Eq. (2) with B_o = 0.5. The vertical dashed lines mark the bounds of the uniform magnetic field region. The vertical dotted line marks where the magnetic field strength goes to zero.

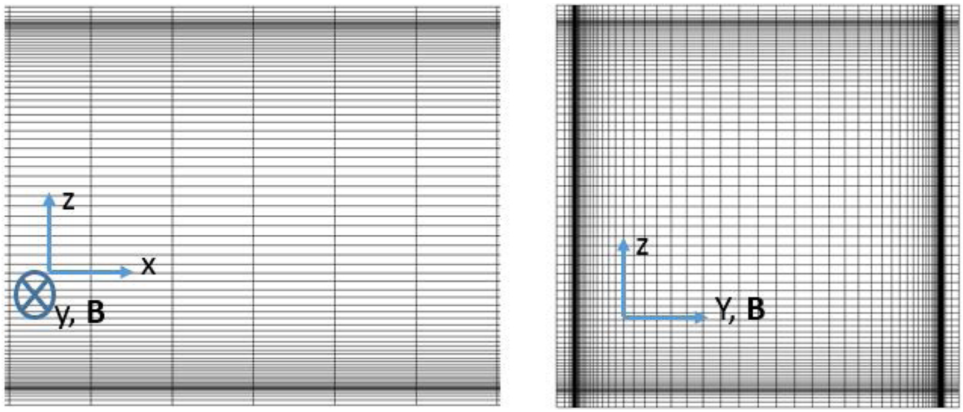

Fig. 3. An example computational mesh with 1510400 cells. Due to the large aspect ratio of x:z, only a small segment of the x axis is included.

via comparison with methods which do not rely on this approximation.

The governing Eqs. (3)–(7) include the continuity equation, momentum equation with the Lorenz force term and the buoyant force term on the right-hand-side, Ohm's law to compute the induced electric current, the electric potential equation, and the thermal energy equation respectively:

$$\nabla \cdot \mathbf{u} = 0, \tag{3}$$

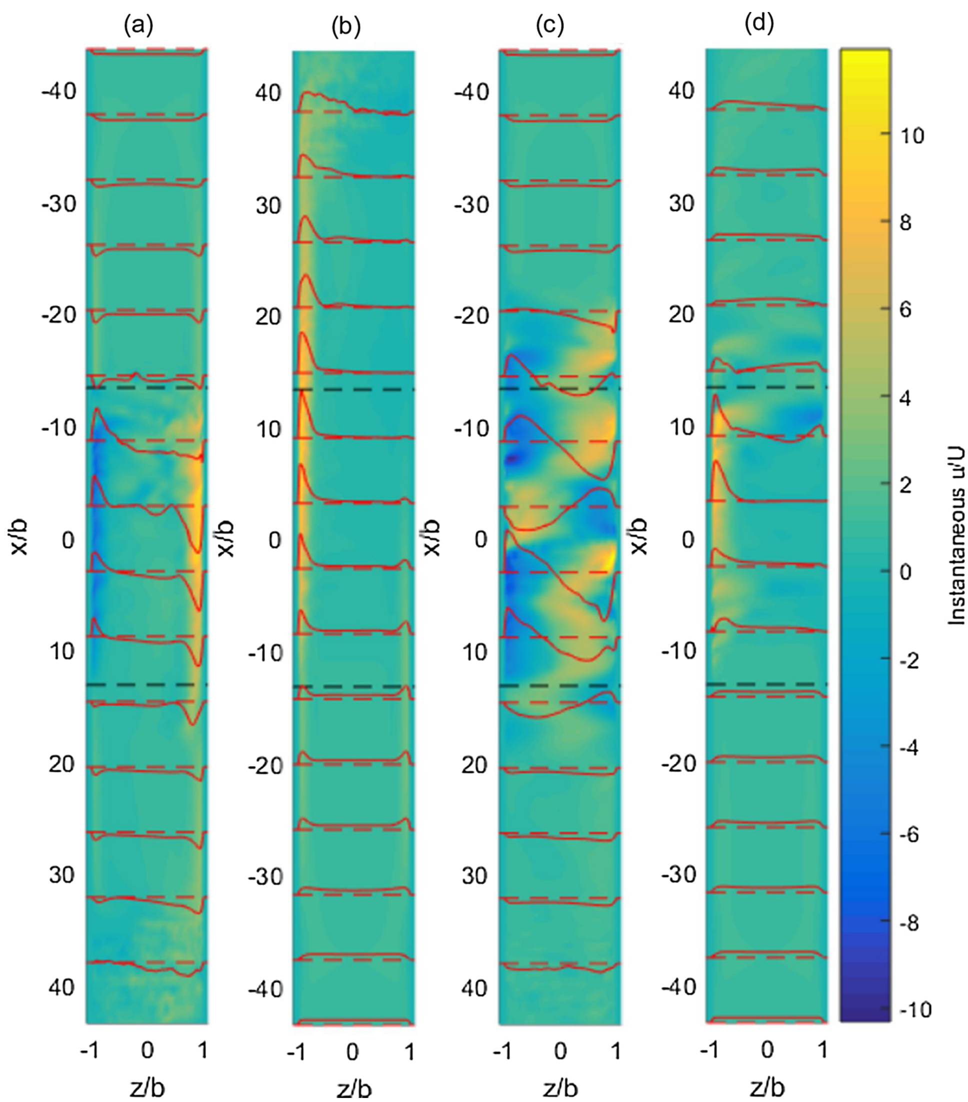

Fig. 4. Instantaneous axial velocity contours and profiles on the y = 0 center-plane. Ha = 220, Re = 2027, Gr = 1.44 × 10^8, surface heating only. (a, b) c_w = 0.12, (c, d) c_w ~ 0. (a, c) Downward flow, (b, d) upward flow. The z-axis is stretched compared to the x-axis by a factor of 5 to more easily view the entire flow field. The dashed, red lines spaced every 5.78 characteristic lengths are the zero lines for the profiles which are solid red lines. The dashed, black lines mark the bounds of the heated region (For interpretation of the references to colour in this figure legend, the reader is referred to the web version of this article.).

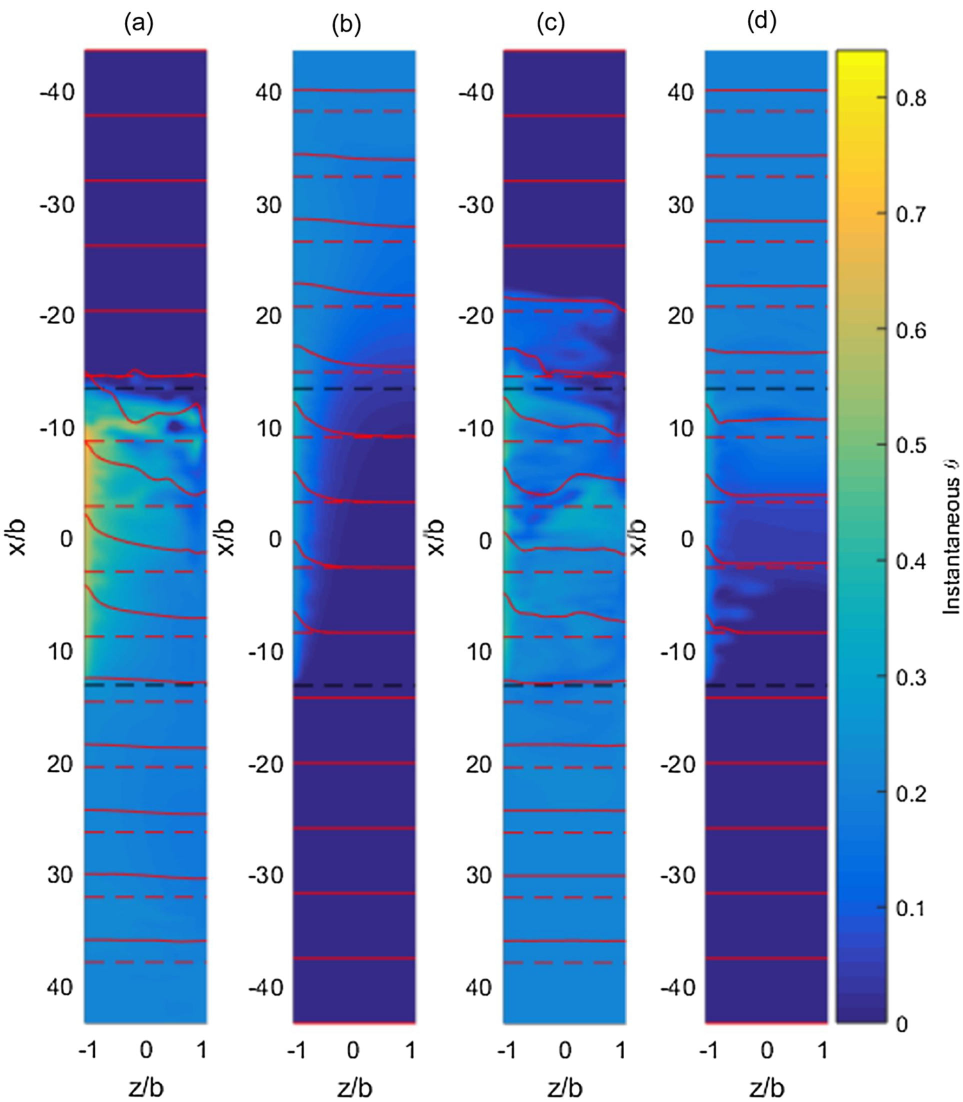

Fig. 5. Instantaneous temperature contours and profiles on the y = 0 center-plane. Ha = 220, Re = 2027, Gr = 1.44×10^8, surface heating only. (a, b) $c_w = 0.12$, (c, d) $c_w \sim 0$. (a, c) Downward flow, (b, d) upward flow. The z-axis is stretched compared to the x-axis by a factor of 5 to more easily view the entire flow field. The dashed, red lines spaced every 5.78 characteristic lengths are the zero lines for the profiles which are solid red lines. The dashed, black lines mark the bounds of the heated region (For interpretation of the references to colour in this figure legend, the reader is referred to the web version of this article.).

$$\frac{\partial \mathbf{u}}{\partial t} + \mathbf{u}\bullet\nabla\mathbf{u} = -\frac{1}{\rho}\nabla\, p + \nabla\bullet(\nu\nabla\mathbf{u}).\,..$$

$$+\frac{1}{\rho}\mathbf{J}\times\mathbf{B} - \mathbf{g}\beta(\mathrm{T}-T_o), \tag{4}$$

$$\mathbf{J} = \sigma(-\nabla\,\phi + \mathbf{u}\times\mathbf{B}), \tag{5}$$

$$\nabla\bullet(\sigma\nabla\phi) = \nabla\bullet(\sigma\mathbf{u}\times\mathbf{B}), \tag{6}$$

$$\rho c_p\left(\frac{\partial \mathrm{T}}{\partial \mathrm{t}} + \mathbf{u}\bullet\nabla\mathrm{T}\right) = \nabla\bullet(k\nabla\mathrm{T}) + q''' . \tag{7}$$

Here, $\mathbf{u}$, $\mathbf{J}$, and $\mathbf{B}$, and $\boldsymbol{g}$ are the velocity, electric current density, magnetic field, and gravity vectors respectively and p, ϕ, and T are the pressure, electric potential, and temperature scalars. T_o is the inlet temperature which is set to 300 °C for all present cases. A term equal to $\boldsymbol{g}$ is omitted from the right-hand side of Eq. (4) as this term would be totally absorbed by the pressure gradient and simply omitting it precludes the need to subtract the static pressure distribution from the results. Eq. (6) is obtained by taking the divergence of Eq. (5) while stipulating that electric current is continuous ($\nabla\bullet\mathbf{J} = 0$). To consider both the liquid and the surrounding solid wall, which may have different electrical conductivity, the electrical conductivity σ is put inside the derivatives in Eq. (6). Similarly for the thermal conductivity in Eq. (7) and the viscosity in Eq. (4).

Eqs. (3)–(7) were solved numerically using direct numerical simulation methods on non-uniform rectangular meshes (Fig. 3). There are at least 8 nodes inside all Hartmann layers on the walls perpendicular to the magnetic field and 10 nodes inside each side layer on the wall parallel to the magnetic field. Lower mesh resolution is used throughout the central region of the duct as it is expected that the magnetic field damps out flow features with small length scales in the bulk of the flow. Where the magnetic field is small or zero, the mesh is still not refined as the smallscale flow behavior in those regions are not a topic of interest in this work. A mesh sensitivity study was performed, and the results are presented in [28].

The inlet velocity boundary condition specifies uniform flow with velocity U at x = -1 m while a fully developed flow outlet boundary condition in the form $\frac{\partial \boldsymbol{u}}{\partial \mathrm{x}} = 0$ is used at the outlet at x = 1.4 m. The no slip and no flow-through conditions are enforced at fluid-wall interfaces ($\mathbf{u_{wall}} = 0$). The pressure is set to zero at the outlet and the fluid-wall boundaries and the inlet have Neumann pressure conditions $\left(\frac{\partial p}{\partial n} = 0\right)$. Normal components of electric current density are set to zero at the

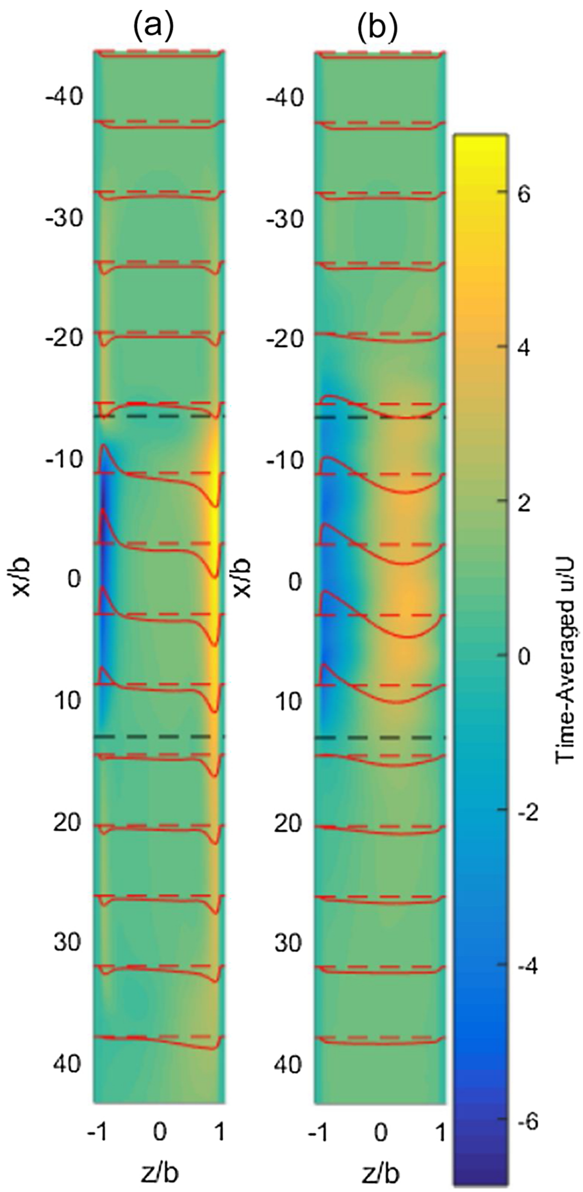

Fig. 6. Instantaneous time-averaged axial velocity contours and profiles on the y = 0 center-plane. Downward flow with surface heating. Ha = 220, Re = 2027, Gr = 1.44 × 10^8. (a) c_w = 0.12, (b) c_w ~ 0. The z-axis is stretched compared to the x-axis by a factor of 5 to more easily view the entire flow field. The dashed, red lines spaced every 5.78 characteristic lengths are the zero lines for the profiles which are solid red lines. The dashed, black lines mark the bounds of the heated region (For interpretation of the references to colour in this figure legend, the reader is referred to the web version of this article.).

outer domain boundary $\left(\frac{\partial\phi}{\partial n} = (\mathbf{u}\times\mathbf{B})\cdot\hat{\boldsymbol{n}}\right)$. Adiabatic conditions $\left(\frac{\partial T}{\partial n} = 0\right)$ are set for all outer domain boundaries except for the inlet, where the temperature is prescribed as $T = T_o = 300\,^{\circ}C$, and, when the applied heating mode is surface heating, the outer boundary of the wall at $z = -a - t_w$, $-b - t_w \le y \le b + t_w$, $-\frac{L_h}{2} \le x \le \frac{L_h}{2}$, has $\frac{\partial T}{\partial z} = -q_o''/k$.

For numerical stability reasons the viscosity of the LM is linearly ramped up artificially from 1 to 1000 times the inlet value over the last 0.4 m of the duct in what is referred to here as the high viscosity outlet region but is otherwise known as a viscous sponge layer [29]. The purpose of this is to quickly develop the flow and to damp out vortices which may otherwise make their way to the outlet. Without a high viscosity outlet region, vortices have been observed to approach and ultimately straddle the outlet thereby adversely affecting the convergence of the numerical solver. Including the high viscosity outlet region fixes this and ensures that the outlet boundary conditions behave properly without the need of an extremely long and prohibitively expensive outlet region.

Simulations were started with initially uniform flow and uniform temperature conditions with initial velocity U and temperature T_o. A time step size of $\Delta t = 10^{-4}$ s was used for all cases. To reduce risk of divergence in the early development of the flow, partial up-winding ($\lambda_u = 0.7$) was used for the first 200,000 timesteps in each case, after which the up-winding factor was set to $\lambda_u = 1.0$ (central differencing/ no up-winding) to restore the 2nd order accuracy of the solver for the remainder of the simulation. Each simulation was run in parallel on 1024 cores on the computing clusters at the National Energy Research Scientific Computing Center (NERSC). Using 1024 cores, the computations proceeded at a rate of ~1 million timesteps per 24 h such that the shortest simulations were finished in ~3 days. MHD mixed convection flows at high Gr numbers are inherently unsteady so the stopping criteria of the simulations is one based on statistical steadiness. Simulations must run long enough to converge (~1.5 million steps), but also to continue running to confirm statistical steadiness (~1.5 million steps) meaning that the time rate of change of time-averaged flow variables goes to zero.

A total of 15 cases were simulated as listed in Table 1. The results shown correspond to those of the final timestep, except where they are averaged from timestep 1e6 to the final time step. As such, results are labeled either "instantaneous" or "time averaged" respectively.

3. Results and discussion

3.1. Features of MHD mixed convection flows in a vertical duct

An overview of the behavior of MHD flow through vertical ducts with applied surface heating and transverse magnetic field is presented in this section to provide context for more detailed parametric and comparison studies in the following sections. Both upward flowing and downward flowing cases are presented for ducts with either conducting or insulating walls, totaling to four flow scenarios. The details of the simulation geometry are defined in Fig. 1 and the nondimensional parameters are $Re = 2027$, $Ha = 220$, $Gr = 1.44 \times 10^8$ for all four scenarios presented in this section with two having $c_w = 0.12$ and the other two having $c_w \sim 0$. The velocity fields on the y = 0 center-plane are provided in Fig. 4. Even though the flow was computed in 3D, the flow structure within the magnetic field region is mostly Q2D with an almost uniform core and thin Hartmann boundary layers at the duct walls perpendicular to the magnetic field. Such a Q2D flow structure is typical to many MHD duct flows in a strong magnetic field, such that plotting the data at the mid-plane is a good way to represent the entire flow. Some discrepancies of the computed flows from the idealized Q2D flow are discussed in section 3.4.

The flow enters as isothermal uniform flow from either the top or the bottom end of the vertical duct.

As the flow proceeds downstream, the flow develops hydrodynamically and a viscous boundary layer begins to grow near the walls, smoothening out the sharp discontinuity of the velocity profile there. The hydrodynamic development is interrupted by the growth of the transverse magnetic field which ramps up quickly downstream.

The effect of a fringing magnetic field (i.e. a magnetic field which is uniform in some region but decays to zero or "fringes" on the periphery of the region) on liquid metal flows has been thoroughly studied in the past (e.g. [30–32]). A 3D electromagnetic disturbance occurs in the vicinity of the fringe. This disturbance is characterized by 3D electrical currents which close along the axial direction. Additionally, a 3D MHD pressure drop is inserted into the flow and the velocity profile becomes M-shaped. This effect is prominent in insulating ducts but is somewhat less important in ducts with conducting walls where the 3D effects are overshadowed by the larger 2D circulations of electrical current which

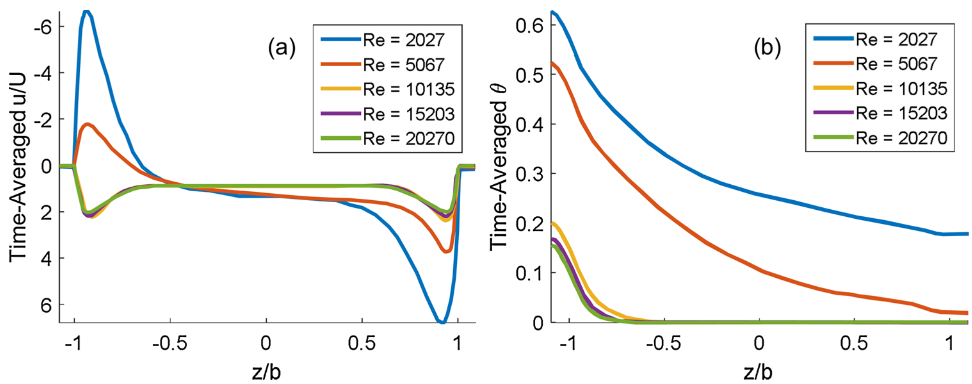

Fig. 7. Profiles of (a) time-averaged axial velocity, and (b) time-averaged temperature along the zdirection at x/b = -4.35 and y/b = 0. Ha = 220, Gr = 1.44×10^8 and c_w = 0.12. Re = 2027, 5067, 10,135, 15,203, and 20,270 for the case of downward flow.

Table 1
Simulation Matrix.

#	Flow Direction	Wall Conductivity	Heating Mode	Ha	Re	Gr	c_w	Final Timestep
1	Down	Conducting	Surface	220	2027	1.44×10^8	0.12	3.4e6
2	Down	Insulating	Surface	220	2027	1.44×10^8	1×10^{-9}	3.5e6
3	Up	Conducting	Surface	220	2027	1.44×10^8	0.12	3.5e6
4	Up	Insulating	Surface	220	2027	1.44×10^8	1×10^{-9}	3.15e6
5	Down	Conducting	Exponential	220	2027	1.57×10^8	0.12	8.1e6
6	Down	Insulating	Exponential	220	2027	1.57×10^8	1×10^{-9}	4.65e6
7	Up	Conducting	Exponential	220	2027	1.57×10^8	0.12	3.235e6
8	Up	Insulating	Exponential	220	2027	1.57×10^8	1×10^{-9}	2.95e6
9[a]	Down	Conducting	Surface	220	5068	5.04×10^7	0.12	3.65e6
10[a]	Down	Conducting	Surface	220	5068	5.04×10^7	0.12	4e6
11[a]	Down	Conducting	Surface	220	5068	5.04×10^7	0.12	2.65e6
12	Up	Conducting	Nuclear	220	2027	1.57×10^8	0.12	2.7e6
13	Up	Insulating	Nuclear	220	2027	1.57×10^8	1×10^{-9}	2.75e6
14	Down	Conducting	Nuclear	220	2027	1.57×10^8	0.12	4.25e6
15	Down	Insulating	Nuclear	220	2027	1.57×10^8	1×10^{-9}	2.9e6

[a] Cases 9–11 are part of a mesh refinement study [28]. They feature the same parameters but three different meshes.

Table 2
Simulation Matrix for Parametric Survey.

#	Flow Direction	Ha	Re	Gr	B [T]	U [m/s]	q_o” [MW/m^2]
1	Down	220	2027	1.44×10^8	0.50	0.02	0.20
2	Up	220	2027	1.44×10^8	0.50	0.02	0.20
3	Down	220	5068	1.44×10^8	0.50	0.05	0.20
4	Down	220	10135	1.44×10^8	0.50	0.10	0.20
5	Down	220	15203	1.44×10^8	0.50	0.15	0.20
6	Down	220	20270	1.44×10^8	0.50	0.20	0.20
7	Down	110	2027	1.44×10^8	0.25	0.02	0.20
8	Down	440	2027	1.44×10^8	1.00	0.02	0.20
9	Down	880	2027	1.44×10^8	2.00	0.02	0.20
10	Down	220	2027	3.6×10^8	0.50	0.02	0.50
11	Up	220	5068	1.44×10^8	0.50	0.05	0.20
12	Up	220	10135	1.44×10^8	0.50	0.10	0.20
13	Up	220	15201	1.44×10^8	0.50	0.15	0.20
14	Up	220	20270	1.44×10^8	0.50	0.20	0.20
15	Up	110	2027	1.44×10^8	0.25	0.02	0.20
16	Up	880	2027	1.44×10^8	2.00	0.02	0.20
17	Up	220	2027	3.6×10^8	0.50	0.02	0.50

close in the conducting walls rather than inside the fluid.

As the flow moves deeper into the region of uniform transverse magnetic field, the 3D disturbance caused by the fringe fades and the flow quickly develops towards classical Shercliff [33] or Hunt flow [34] for the case of insulating and conducting ducts respectively. Both fully developed flows feature nearly uniform velocity in the “bulk” – a central region which includes the vast majority of the duct’s cross-section. The flow in the bulk is characterized by a dominance of electromagnetic Lorentz force ($=\mathrm{J}\times\mathbf{B}$) which is balanced by the pressure gradient. The bulk is framed by special layers attached to the walls inside which viscous forces are significant. Layers attached to walls perpendicular to the transverse magnetic field are “Hartmann layers” and have thickness which scales inversely with the Hartmann number. Layers attached to walls parallel to the magnetic field are “side layers” and have thickness which scales with the inverse of the square-root of Hartmann number.

Further downstream, buoyancy becomes important as the flow is no longer isothermal. The instantaneous temperature distribution is shown for each of the four scenarios in Fig. 5. In the upward flow cases, the flow remains isothermal until entering the heated region at $x/b = -13.25$ since the heat is advected downstream much faster than it can conduct upstream; however, in the downward flow cases, buoyant flow structures advect heat upstream of the heated region, most notably in the case of insulating walls where elevated temperatures are observed as far as $\sim x/b = -22$, well upstream of the entrance to the heated region.

Wherever the buoyant force field has nonzero curl, pressure is not able to balance it and so the velocity field is forced to adapt to give rise to rotational electromagnetic and/or hydrodynamic forces. As such, the flow tends to demonstrate patterns typical to rotational flows, such as inflection points in the velocity profile, formation of high-velocity jets and associated internal shear layers. Furthermore, buoyant effects tend to destabilize the flow. As shown in Figs. 4 and 5, velocity and temperature fluctuations are present where the flow cross-sections are non-isothermal. These fluctuations are partially suppressed by toggling the wall conductivity from insulating to conducting due to the conducting wall cases having stronger Joule dissipation which tends to stabilize flow by dissipating kinetic energy into heat due to strong induced currents closing through the walls.

Strongly **buoyancy opposed flows** (downward flows) are characterized by the detachment of the side layer from the heated sidewall,

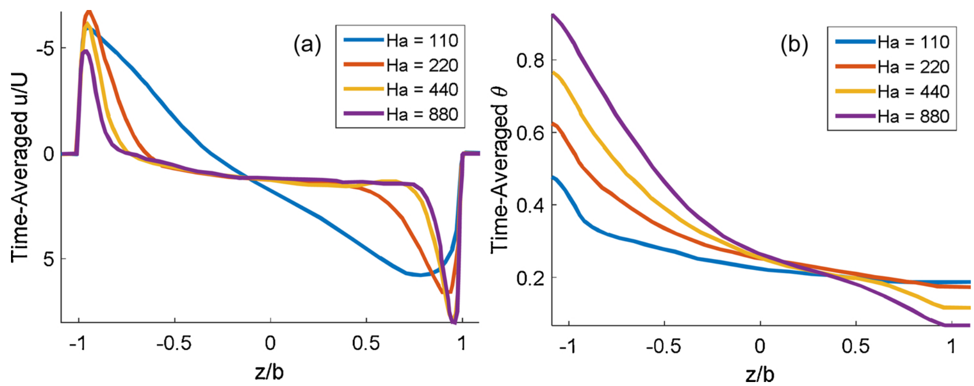

Fig. 8. Profiles of (a) time-averaged axial velocity, and (b) time-averaged temperature along the zdirection at x/b = -4.35 and y/b = 0 for Re = 2027, Gr = 1.44×10^8 and c_w = 0.12. Ha = 110, 220, 440, and 880.

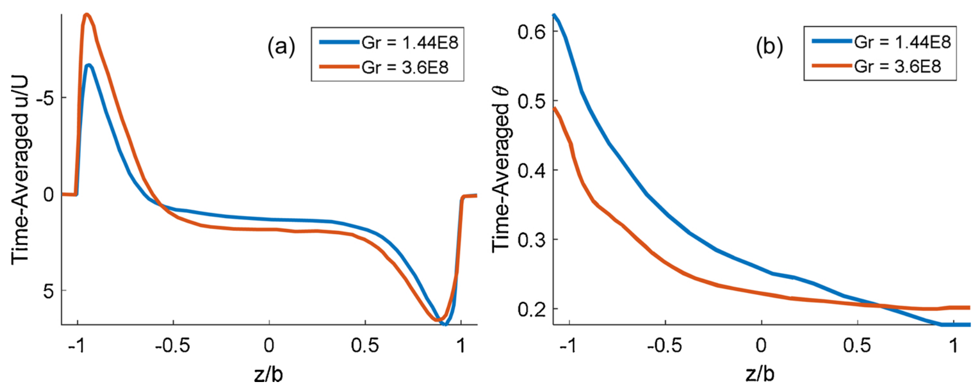

Fig. 9. Profiles of (a) time-averaged axial velocity, and (b) time-averaged temperature along the zdirection at x/b = -4.35 and y/b = 0 for Ha = 220, Re = 2027, and c_w = 0.12 for downward flow. Gr = 1.44×10^8, 3.6×10^8.

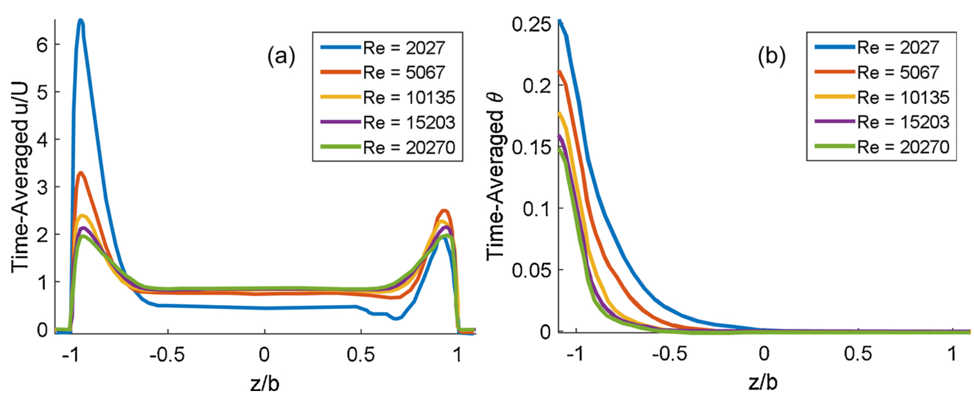

Fig. 10. Profiles of (a) time-averaged axial velocity, and (b) time-averaged temperature along the zdirection at x/b = -4.35 and y/b = 0. Ha = 220, Gr = 1.44×10^8 and c_w = 0.12. Re = 2027, 5067, 10,135, 15,203, and 20270.

followed by a region of reverse flow that spans the length of the heated region near the hot sidewall. By time-averaging the velocity field (Fig. 6), it can be seen that generally, the flow recirculates inside the heated region, moving up on the hot side and down on the cold side, with maximum speeds several times larger than the forced flow mean speed.

Strongly **buoyancy assisted flows** (upward flows) are characterized by the development of a buoyant jet attached to the heated wall. As the flow moves further into the heated region and the temperature of the hot wall increases, the portion of the flow carried by the buoyant jet increases to ~100 % of the total flowrate while the flow stagnates or recirculates weakly away from the hot sidewall. Significant velocity fluctuations in the jet are observed in the case of insulating walls as a wavelike instability grows along the axial direction, culminating in large vortices which span the entire thickness of the duct. The instability mechanism is KelvinHelmholtz instability as it often happens in MHD flows with an inflection point in the velocity profile [18]. This instability is fully suppressed or reduced in the case of conducting walls, likely due to increased Joule dissipation.

Downstream of the heated region, the flow slowly tends to redevelop towards Shercliff and Hunt flows. This development is limited by the rate of heat transfer inside the fluid. This results in a large development length required for the flow to become isothermal and fully developed and so the velocity field remains asymmetrical.

Near the outlet of the duct, the magnetic field ramps down, causing a 3D disturbance similar to the one near the entrance to the magnetic field region.

As the magnetic field disappears, the flow transitions to turbulence.

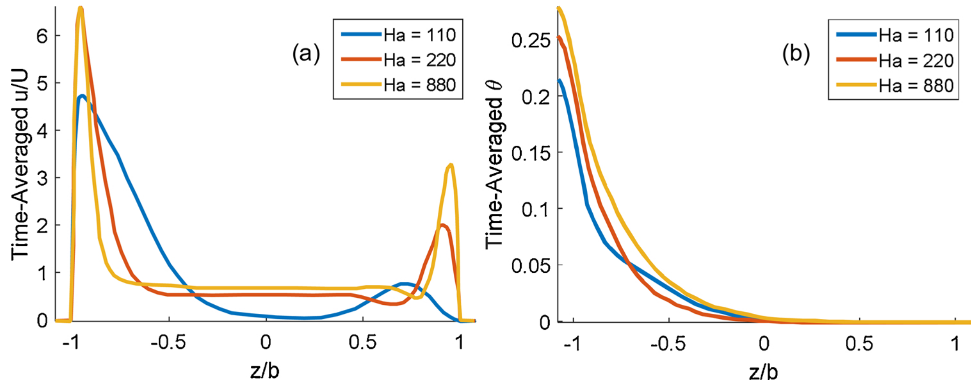

Fig. 11. Profiles of (a) time-averaged axial velocity, and (b) time-averaged temperature along the zdirection at x/b = -4.35 and y/b = 0 for Ha = 220, Re = 2027, and c_w = 0.12 for upward flow. Ha = 110, 220, and 880.

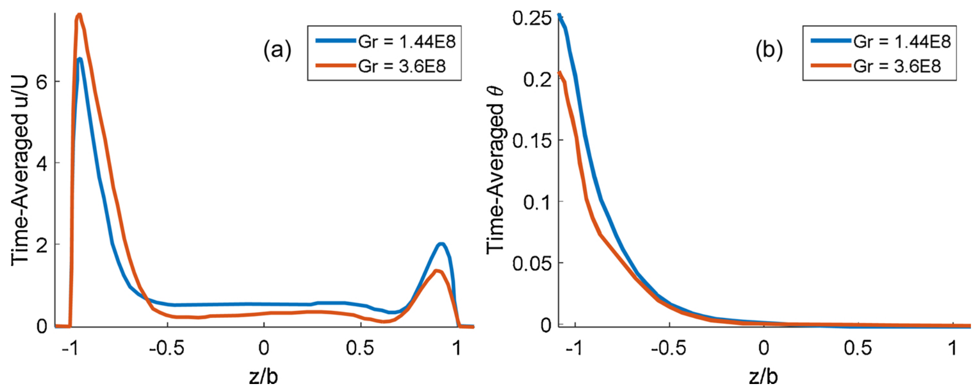

Fig. 12. Profiles of (a) time-averaged axial velocity, and (b) time-averaged temperature along the zdirection at x/b = -4.35 and y/b = 0 for Ha = 220, Re = 2027, and c_w = 0.12 for upward flow. Gr = 1.44×10^8, $3.6 \times 10^{8.}$

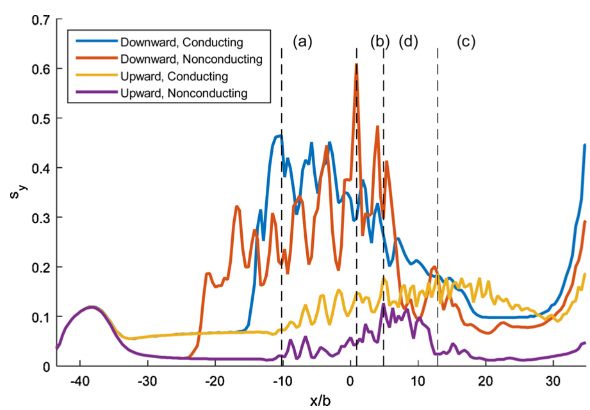

Fig. 13. y-nonuniformity of the instantaneous axial velocity field on fluid cross-sections for each of 4 cases with surface heating and variable flow orientation (upwards or downwards) and wall conductivity (c_w = 0.12 or ~0). Ha = 220, Re = 2027, Gr = 1.44×10^8. The locations where y-nonuniformity is maximum are marked by black dotted lines (a)-(d) for (a) downward flow in a conducting duct, (b) downward flow in a insulating duct, (c) upward flow in a conducting duct, and (d) upward flow in a insulating duct.

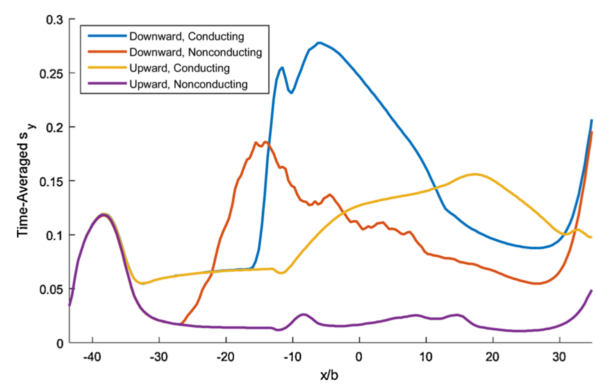

Fig. 14. y-nonuniformity of the time-averaged axial velocity field on fluid cross-sections for each of 4 cases with surface heating and variable flow orientation (upwards or downwards) and wall conductivity (c_w = 0.12 or ~0). Ha = 220, Re = 2027, Gr = 1.44×10^8.

Or rather, it would be turbulent, but the mesh is not fine enough to properly capture the fluctuations which occur over very small length scales (e.g. the Kolmogorov scale). Still, strongly 3D fluctuations are present in this region. As a result of these fluctuations, the flow rapidly becomes isothermal. The unphysical nature of this region does not affect the upstream flow. Lastly, inside the high viscosity outlet, flow undergoes rapid laminarization and subsequent development before exiting the duct as fully developed hydrodynamic flow.

3.2. Effect of Ha, Re, and Gr, on vertical flows in a conducting duct

To test the effect of Hartmann (Ha=110-880), Reynolds (Re=202720270), and Grashof (Gr=1.44×10^8, 3.6×10^8) numbers on the behavior of MHD mixed convection flows in vertical ducts (Fig. 1), 17 case were simulated (Table 2). In all cases, c_w = 0.12.

To support the findings of the parametric study, a dimensionless version of the governing equations are provided for the particular case of constant thermophysical properties, shown below as Eqs. (8-12), using the MHD scale for pressure ($[p] = [\sigma U B^2 L]$):

$$\nabla^* \bullet \mathbf{u}^* = 0, \quad (8)$$

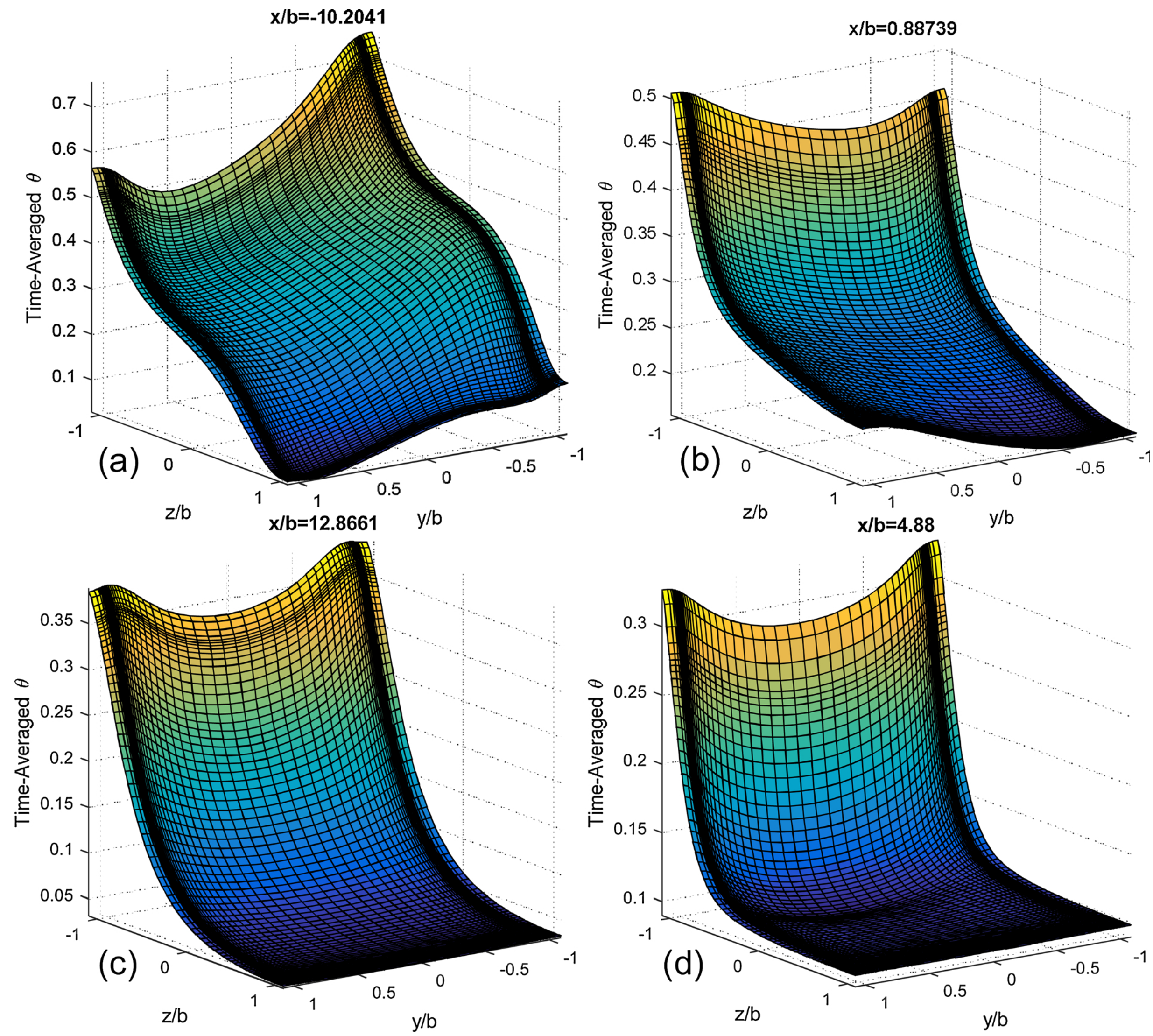

Fig. 15. 2D profiles of the time-averaged temperature field on duct cross-sections where the y-nonuniformity is maximum for Ha = 220, Re = 2027, Gr = 1.44 × 10^8, surface heating, (a, c) c_w = 0.12, (b, d) $c_w \sim 0$, and (a, b) downward flow, (c, d) upward flow.

$$Re\left(\frac{\partial \mathbf{u}^*}{\partial t^*} + \mathbf{u}^*\bullet\nabla^*\mathbf{u}^*\right) = -Ha^2\nabla^* p^* + \nabla^{*2}\mathbf{u}^* + Ha^2\mathbf{J}^*\times\mathbf{B}^* - Gr\hat{\mathbf{g}}\,\theta, \tag{9}$$

$$\mathbf{J}^* = (-\nabla^*\phi^* + \mathbf{u}^*\times\mathbf{B}^*), \tag{10}$$

$$\nabla^{*2}\,\phi = \nabla^*\bullet(\mathbf{u}^*\times\mathbf{B}^*), \tag{11}$$

$$\left(\frac{\partial T^*}{\partial t^*} + \mathbf{u}^*\bullet\nabla^*\theta\right) = \frac{1}{PrRe}\nabla^{*2}\,\theta + q'''^*. \tag{12}$$

Here, $\theta = (T - T_0)/\Delta T$.

3.2.1. Effect of Reynolds number in downward flows

Five downward flow simulations were performed with $Ha = 220$, $Gr = 1.44 \times 10^8$ and various Reynolds numbers ranging from 2027 to 20270. The lower Re flows feature prominent flow reversal in the heated region (Fig. 7a), though the reverse flow is severely diminished at $Re = 10{,}135$ and nonexistent in the higher Re flows. As Re increases, the flow regime shifts into a purely forced convection MHD regime where the effect of the buoyant forces are negligible and the velocity profiles are symmetrical. At low Re, the hot wall temperature becomes very large ($\theta \sim 0.6$) compared to high Re cases ($\theta \sim .15$) due to the recirculation of warm fluid in the low Re cases. In the forced convection MHD regime, increasing Re decreases the temperature more slowly than in the MHD mixed convection regime (Fig. 7b).

3.2.2. Effect of Hartmann number in downward flows

Four downward flow simulations were performed with $Re = 2027$, $Gr = 1.44 \times 10^8$ and various Hartmann numbers ranging from 110 to 880. As Ha increases, the strength of the reverse flow decreases slightly and the jets attached to the sidewalls become thinner (Fig. 8a). Also, the temperature difference between the cold and hot walls increases (Fig. 8b) due to the improved stability of the flow afforded by stronger electromagnetic effects. At $Ha = 110$, the velocity profile does not feature thin jets attached to the wall because the MHD effects are overshadowed by comparatively larger natural convection effects.

3.2.3. Effect of Grashof number in downward flows

Two downward flow simulations were performed with $Ha = 220$, $Re = 2027$, and two Grashof numbers, 1.44×10^8 and 3.6×10^8. In the case of $Gr = 3.6 \times 10^8$, the reverse flow is comparatively larger than in the case of $Gr = 1.4 \times 10^8$ (Fig. 9a) and the temperature solution upstream of the heated region is disturbed by the buoyancy-driven reverse flow. By increasing Gr, the dimensionless temperature increase θ of the hot wall measured at $x/b = -4.35$ (Fig. 9b) decreases by 0.14, despite having stronger flow reversal. This decrease indicates stronger convective heat transfer away from the hot wall, likely due to larger flow

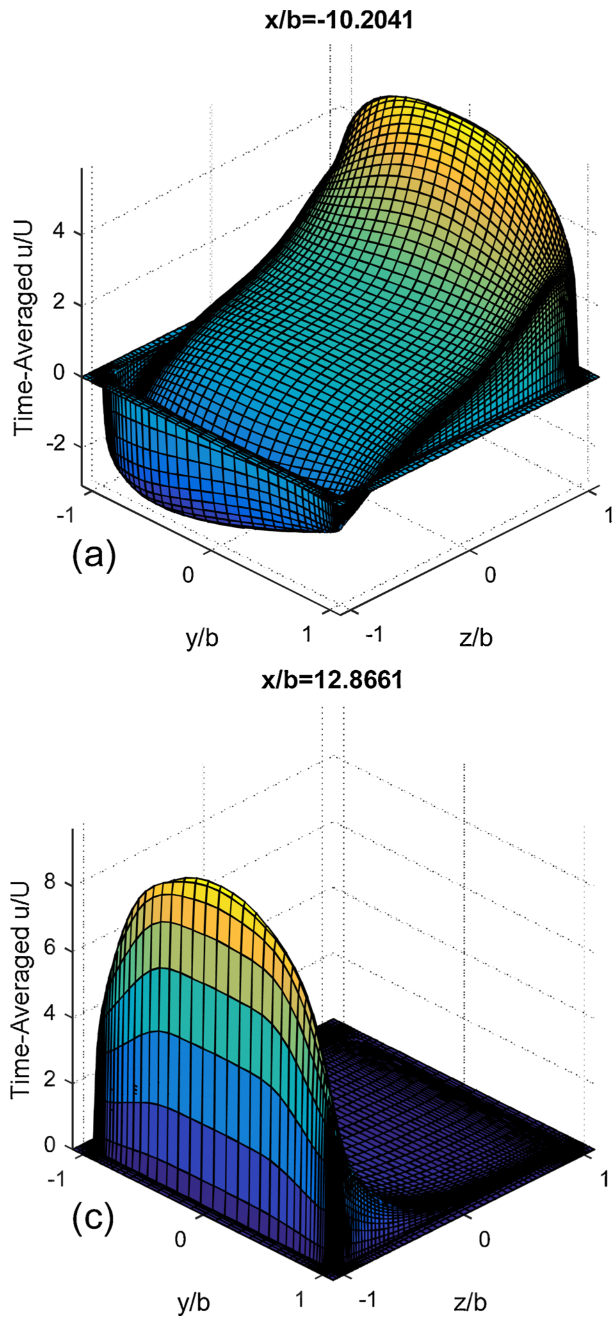

Fig. 16. 2D profiles of the time-averaged velocity field on duct cross-sections where the y-nonuniformity is maximum for Ha = 220, Re = 2027, Gr = 1.44×10^8, surface heating, (a, c) c_w = 0.12, (b, d) $c_w \sim 0$, and (a, b) downward flow, (c, d) upward flow.

instability at higher *Gr*.

3.2.4. Effect of Reynolds number in upward flows

Five upward flow simulations were performed with *Ha* = 220, *Gr* = 1.44×10^8 and various Reynolds numbers ranging from 2027 to 20270. The most prominent effect of buoyancy shown in Fig. 10 is the asymmetry of the velocity profiles; the hot wall features forward flow jets which are faster than the jets on the cold wall. As *Re* increases, this asymmetry fades until velocity profile is symmetrical and the regime is that of MHD forced flow rather than MHD mixed convection flow. Increasing *Re* also decreases both the thermal boundary layer thickness and the maximum temperature (Fig. 10b) by consequence of increased convection along the flow direction.

3.2.5. Effect of Hartmann number in upward flows

Three upward flow simulations were performed with *Re* = 2027, *Gr* = 1.44×10^8 and various Hartmann numbers ranging from 110 to 880. Increasing *Ha* causes larger maximum temperatures at the hot wall (Fig. 11b). This indicates weaker convective heat transfer away from the hot wall explained by the tendency for strong MHD effects to improve flow stability. Additionally, the jets attached to the sidewalls become thinner and the bulk flow becomes more uniform as *Ha* increases (Fig. 11a).

3.2.6. Effect of Grashof number in upward flows

Two upward flow simulations were performed with *Ha* = 220, *Re* = 2027, and two Grashof numbers, 1.44×10^8 and 3.6×10^8. In the case of *Gr* = 3.6×10^8, the jet attached to the hot wall is faster than in the case of *Gr* = 1.44×10^8 due to stronger buoyancy effect (Fig. 12a).

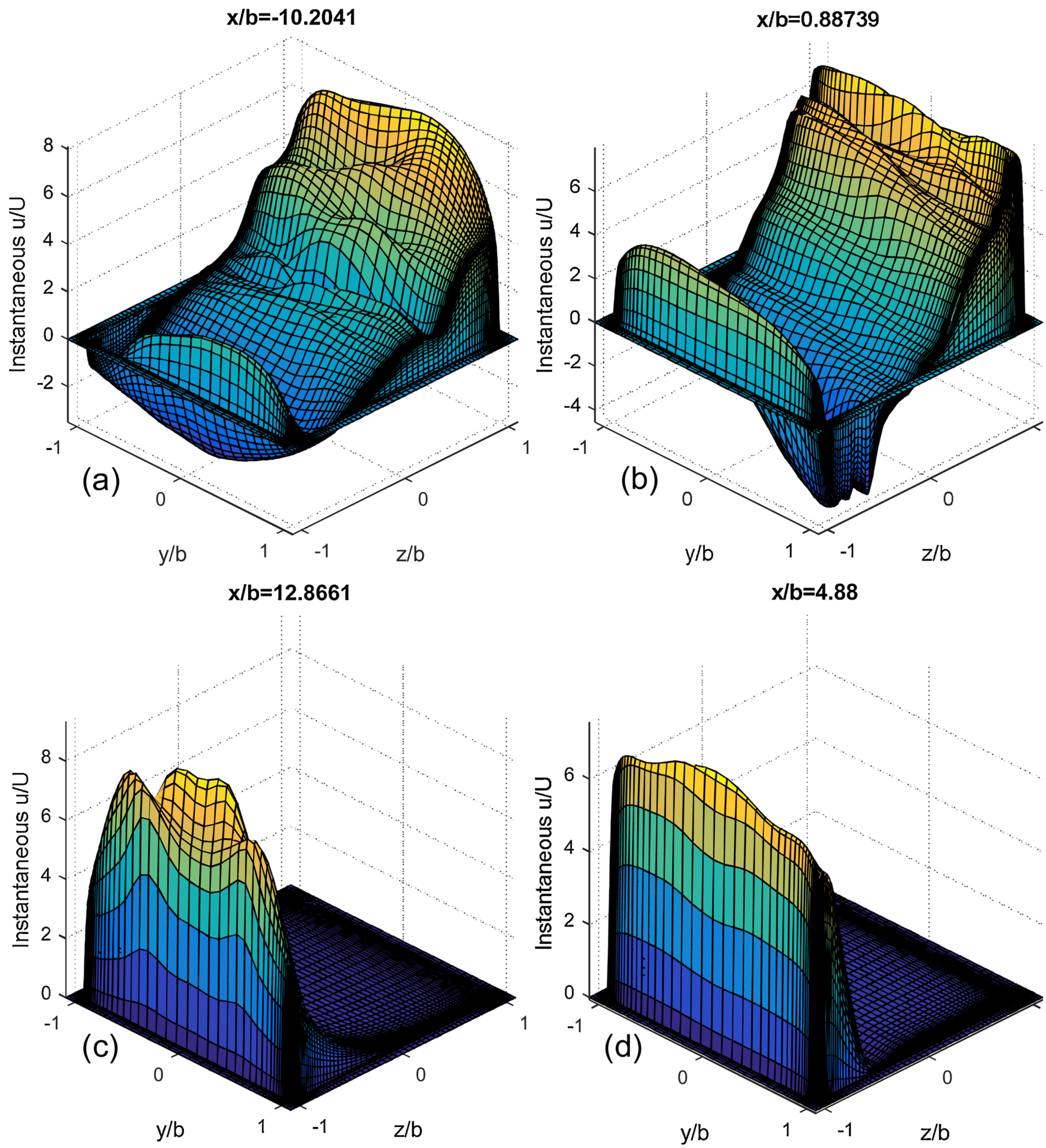

Fig. 17. 2D profiles of the instantaneous velocity field on duct cross-sections where the y-nonuniformity is maximum for Ha = 220, Re = 2027, Gr = 1.44×10^8, surface heating, (a, c) $c_w = 0.12$, (b, d) $c_w \sim 0$, and (a, b) downward flow, (c, d) upward flow.

Increasing *Gr* causes the dimensionless temperature to decrease at the hot wall (Fig. 12b), indicating stronger convective heat transfer away from the hot wall.

3.3. 3D flow features

The results of four cases (#14 in Table 1) consisting of upwards and downwards flows in both conducting and insulating ducts with surface heating in the setup described in Section 2 (Fig. 1) were examined for $Ha = 220$, $Re = 2027$, $Gr = 1.44 \times 10^8$. In the following analysis, the means by which the buoyant forces diminish the Q2D quality of the flow is explored; however, one should note that the turbulence is still not isotropic due to the effects of Joule dissipation.

The following metric is proposed for evaluating how nonuniform a flow's velocity distribution is along the y-direction. The y-nonuniformity metric, s_y, is evaluated at each crosssection along the axis as in Eq. (13):

$$s_y(x, t) = \frac{\sum_i \Delta z_i \sum_j \Delta y_j \, |u_{ij}(x, t) - \bar{U}_{y_i}(x, t)|}{AU} \tag{13}$$

Here, $\bar{U}_{y_i} = \frac{\int_{-b}^{b} u dy}{\int_{-b}^{b} dy}$ is the velocity averaged across y at each z location denoted by the subscript, i. The subscript j corresponds to grid locations along the y direction. Δz_i and Δy_j are grid cell widths, U is the mean velocity, and A is the area.

s_y is plotted for upwards and downwards flows with both conducting and insulating walls in Fig. 13. From the inlet, s_y increases as the initially uniform flow hydrodynamically develops viscous boundary

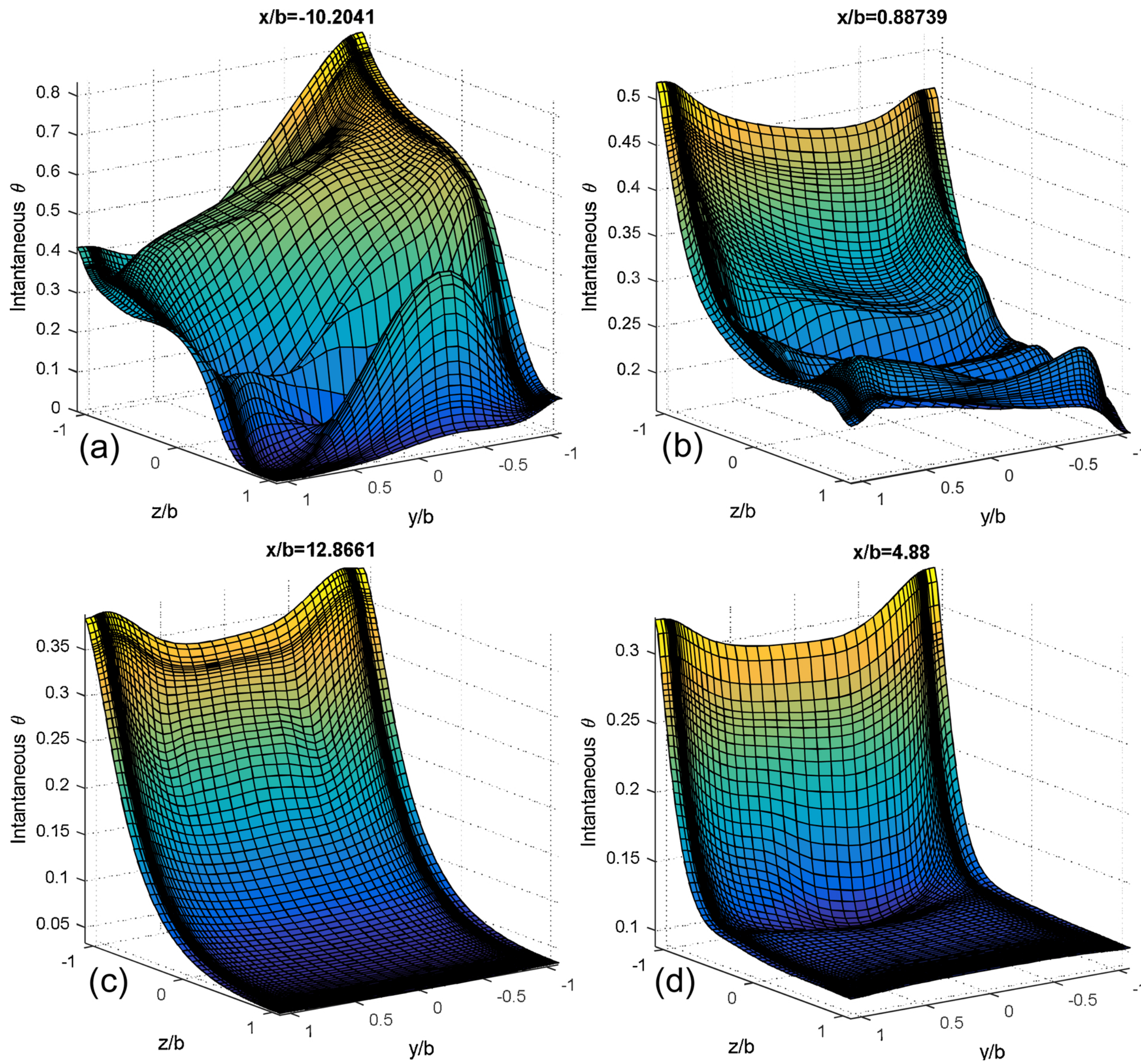

Fig. 18. 2D profiles of the instantaneous temperature field on duct cross-sections where the y-nonuniformity is maximum for Ha = 220, Re = 2027, Gr = 1.44×10^8, surface heating, (a, c) $c_w = 0.12$, (b, d) $c_w \sim 0$, and (a, b) downward flow, (c, d) upward flow.

layers. This is interrupted by the magnetic field ramping up which causes the flow to redistribute evenly along the magnetic field direction outside of very thin MHD boundary layers. The Shercliff and Hunt velocity profiles ($x/b \sim$ -20) feature $s_y = 0.01$ and 0.07 respectively with the latter having a higher value due to the parabolic shape of the side-layer jets. The value of s_y increases in the heated region, especially in the downward flow cases. The increase in s_y can be explained by a combination of 3 proposed effects: (1) buoyancy may shape the velocity field to promote flow instability and inertial transfers of momentum, a competing mechanism to Joule dissipation that acts to restore isotropic turbulence [35]; (2) the temperature profile may be asymmetrical along the magnetic field direction, resulting in asymmetrical velocity profiles necessary to balance the buoyant force; and (3) buoyancy may increase the flow rate inside the side layers where, in conducting ducts, the velocity profile is significantly rounded by viscous forces. These effects will be addressed in the context of the base flow before examining the full unsteady flow.

The so-called “time-averaged s_y” is calculated from replacing the flow variables in Eq. (13) with the time-averaged flow variables. The time-averaged s_y is plotted in Fig. 14.

Except for the upwards conducting case, the time-averaged s_y is generally less than the instantaneous s_y which indicates that the base flow is generally more uniform along the ydirection than any instant of the full unsteady flow. As shown in Figs. 13 and 14, inside the heated region, the buoyancy opposed flows have higher s_y than their upward flow counterparts, and the conducting duct flows have higher s_y than insulating ducts with the same orientation.

Interestingly, the downward cases feature lasting temperature difference between the Hartmann walls which has caused the base velocity profiles to slope along the y-direction. Such stable asymmetry is only possible in the downward scenarios because a feedback relationship exists between velocity and temperature which behaves oppositely in upward scenarios. In (upward) buoyancy assisted flows, the velocity of slightly warmer fluid increases which cools the hot spot and restores temperature uniformity. However, in buoyancy opposed flows, the velocity of relatively warmer fluid decreases which causes the temperature to increase until an asymmetric temperature statistical equilibrium is reached. This asymmetry is observed in the timeaveraged temperature profiles shown below in Fig. 15 which correspond to the location of maximum instantaneous s_y in Fig. 13.

The timeaveraged temperature profiles reveal 25 % and 12 % differences in θ between Hartmann walls for conducting and insulating

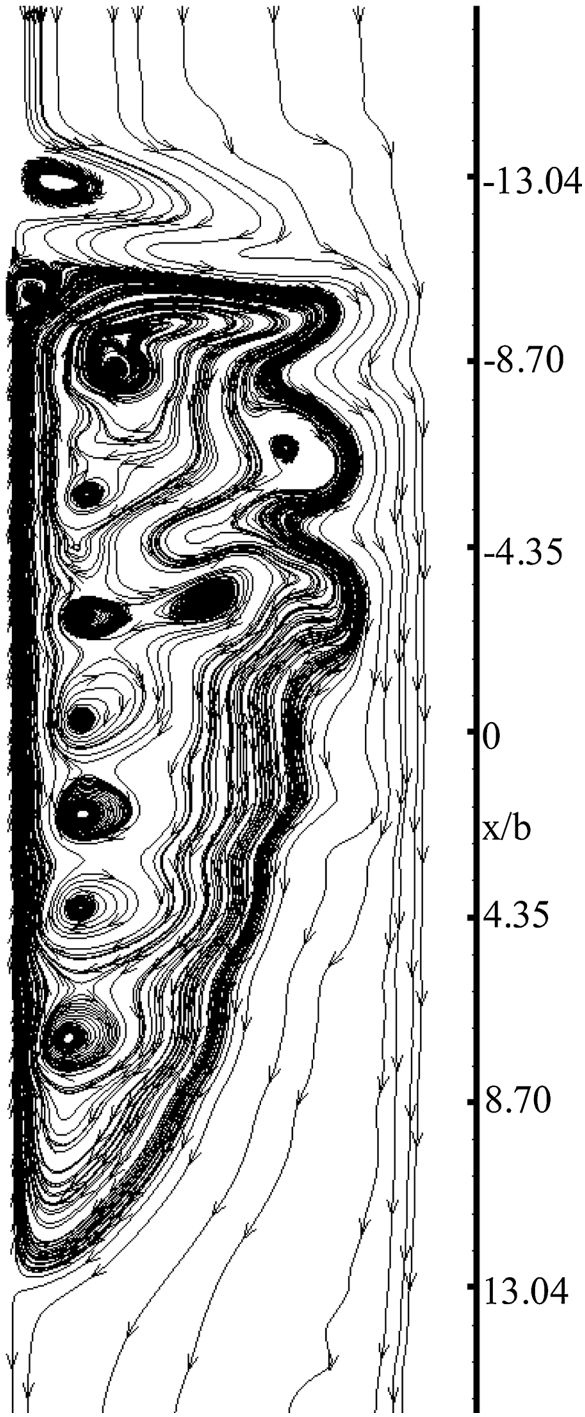

Fig. 19. Velocity streamlines on the y = 0 center-plane for downward flow with surface heating, Ha = 220, Re = 2027, Gr = 1.44 × 10^8, and c_w = 0.12.

walls respectively for downward flows despite the symmetry of the problem setup. There is no significant asymmetry in upward scenarios. The timeaveraged velocity profiles corresponding to the same locations are plotted below in Fig. 16.

The velocity asymmetry due to temperature asymmetry is observed above for the downward cases. Thus, the fact that downward base flows have generally higher flow nonuniformity than upwards base flows can be attributed to this proposed feedback mechanism that promotes asymmetric temperature profiles. Fig. 16 also shows how the base flows in conducting ducts have rounded velocity profiles near the sidewalls while the flows in insulating ducts do not. In locations where buoyant

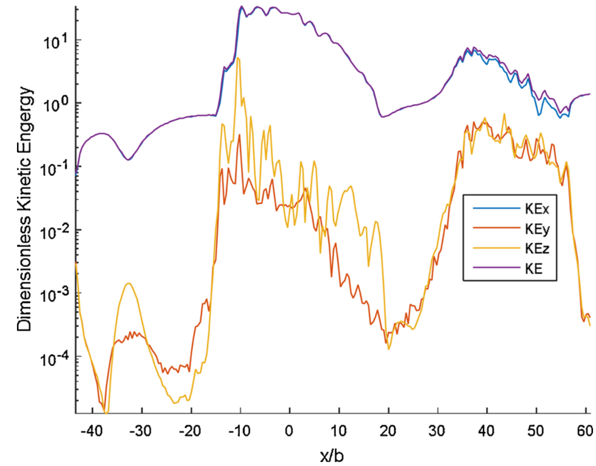

Fig. 20. Total kinetic energy and components of kinetic energy are calculated for fluid cross-sections along the x-direction for downward flow with surface heating, Ha = 220, Re = 2027, Gr = 1.44 × 10^8, and c_w = 0.12. The kinetic energy calculations do not include the mean axial flowrate.

forces are strongest, the jets are largest which accounts for the increased y-nonuniformity in the heated region of conducting ducts.

The nonuniformity along the magnetic field direction is contributed to by unsteady flow features as observed in the oscillations of s_y in the heated region (Fig. 13). The oscillations of s_y have amplitudes of ~0.1 for downward flows and ~0.05 for upward flows indicating stronger ynonuniformity associated with turbulence in buoyancy opposed flow. The axial velocity profiles are provided in Fig. 17 for locations where s_y is largest inside the uniform magnetic field region at the instants shown.

The four axial velocity profiles in Fig. 17 show that the sources of ynonuniformity go beyond the mechanisms which were introduced in the base flow analysis. As shown in the corresponding temperature profiles below (Fig. 18), the y-nonuniformity in temperature is even stronger than in the base temperature field with a 50 % difference in θ between Hartmann walls in the conducting downward case. While the unsteady temperature asymmetry certainly contributes to y-nonuniformity, there are y-nonuniformities in the above velocity profiles which appear independent of the temperature asymmetry. These fluctuations can be explained by the presence of flow instabilities in which inertial forces transfer momentum in all three dimensions.

In downward flows where s_y is largest due to strong fluctuations, there are two modes of instability to consider: (1) shear instability which requires an inflection point in the velocity profile and (2) buoyant instability which requires that the temperature increase in the direction of gravity. In the conducting wall reference case, the shear instability is prevalent throughout the heated region while the buoyant instability mode dominates the insulating duct flow.

Streamlines for the conducting downward flow case are shown in Fig. 19. In transitioning between the forced flow velocity profile to the MHD mixed convection profile with flow reversal, the boundary layer separates from the heated surface and the oncoming flow migrates to the cold sidewall. The transition region beginning at the boundary layer separation is 3.45 characteristic lengths and includes a smaller region of 1.3 lengths where a distinct spike in z-direction kinetic energy and steep increase in xdirection kinetic energy (Fig. 20) occurs as the flow migrates to the cold sidewall. Actually, in the instant depicted, the boundary layer separates in two locations but quickly reattaches downstream of the first location. The disturbance caused by the second (and lasting) separation is shown to coincide with the location of both the maximum y-direction kinetic energy and maximum s_y (x/b = -10.2).

Streamlines for the insulated downward flow case are shown in Fig. 21. With less Joule dissipation than the conducting case, the flow is more unstable and large vortices span the width of the duct for the entire heated region and even 8.7 characteristic lengths upstream and

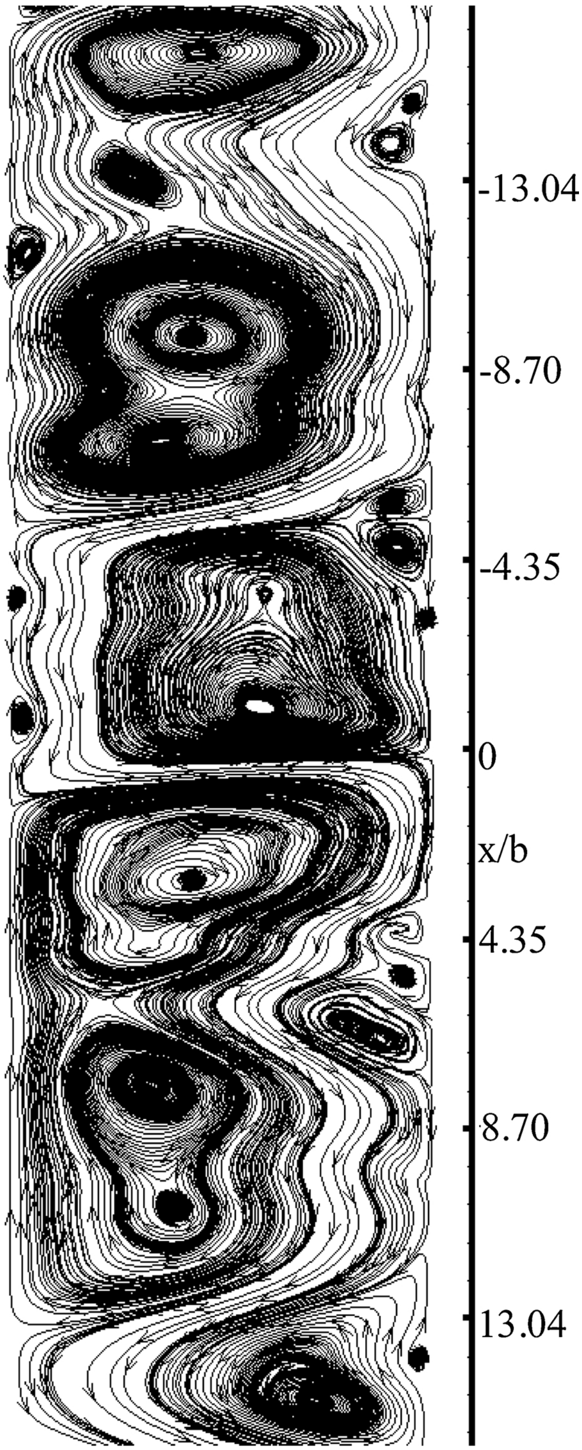

Fig. 21. Velocity streamlines on the y = 0 center-plane for downward flow with surface heating, Ha = 220, Re = 2027, Gr = 1.44 × 10^8, and $c_w \sim 0$.

downstream of the heated region. These large bulk vortices, hallmarks of MHD turbulence, alternate between clockwise and counterclockwise. The boundary layer separates frequently and flow migrates to the opposite sidewall to avoid flowing counter to the circulation of the vortices. As in the conducting scenario, the boundary layer separations coincide with spikes in s_y, and y and z-direction kinetic energy, the largest of these occurring at x/b = 0.89. Though boundary layer separation coincides with the strongest fluctuations of kinetic energy and nonuniformity, fluctuations of these quantities exist throughout the turbulent heated region.

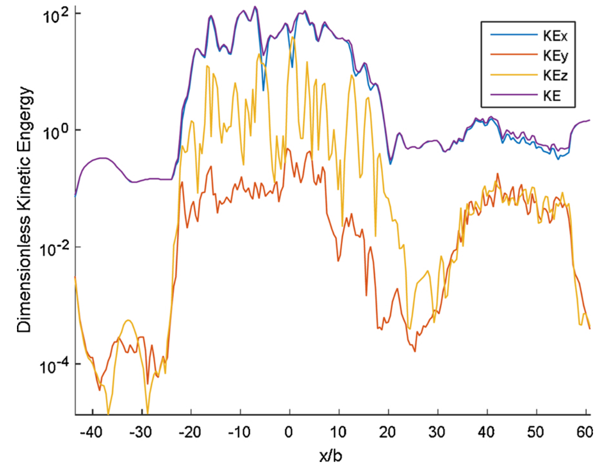

Fig. 22. Total kinetic energy and components of kinetic energy are calculated for fluid cross-sections along the x-direction for downward flow with surface heating, Ha = 220, Re = 2027, Gr = 1.44 × 10^8, and $c_w \sim 0$. The kinetic energy calculations do not include the mean axial flowrate.

It is important to note that in both conducting and insulating scenarios, the kinetic energy associated with z-direction motions is everywhere larger than kinetic energy associated with y-direction motions, and x-direction motions have larger energy still (Fig. 22).

The fluctuations of the conducting and insulating can also be compared via the turbulent kinetic energy and each component of turbulence intensity at multiple points in the flow (Tables 3 and 4). The turbulent kinetic energy (TKE) k is defined in Eq. (14):

$$k = \frac{1}{2}(\bar{u'^2} + \bar{v'^2} + \bar{w'^2}) \tag{14}$$

Where u', v', and w' are defined as $u'(t) = u(t) - \bar{u}$ (and similarly for the y and z components) and the bars over the variables indicate averaging over time. The turbulence intensity I is defined in Eq. (15).

$$I_x = \sqrt{\bar{u'^2}}/U \tag{15}$$

Where u' is replaced with v' or w' to calculate the y and z components of turbulence intensity respectively.

Every value in Table 4 is greater than the corresponding values in Table 3, indicating stronger turbulence in the case of insulating walls. Also, the x and z components of turbulence intensity are each greater than the respective y components, in most cases by an order of magnitude or more, which further supports the claim that the flows exhibit Q2D turbulence.

3.4. Volumetric heating

Eight simulations were performed to study the effect of volumetric heating on MHD flows in vertical ducts as compared to surface heating. Both upwards and downwards flows inside conducting and insulating duct walls were considered. The Ha = 220, Re = 2027, and total heating per axial length Q' = 0.01 MW/m (and thus Gr = 1.57 × 10^8) are the same for all eight cases. In the first four cases, a volumetric nuclear heating profile was used. In the second set of four cases, an exponential heating profile was used that is much steeper than the nuclear heating profile such that nearly all of the heating occurs very near to the sidewall at $z = -a$. In all eight cases, the volumetric heating occurs inside the fluid domain only. Lastly, the volumetric heating cases are compared with surface heating cases with the same Q' to qualify the use of surface heating in studying MHD flows with steep volumetric heating profiles.

The volumetric heating curve of a fusion blanket depends not only on the breeder material but also on the structure and cooling scheme of the blankets. Indeed, the geometry of the reactor and even the shape of

Table 3
Turbulent Characteristics for Downward Flow with Conducting Walls.

(x/b, y/b, z/b)	TKE [m^2/s^2]	Turbulence Intensity x	Turbulence Intensity y	Turbulence Intensity z
(-15.43, 0.25, -0.75)	1.06E-05	0.2138	0.0484	0.0695
(-15.43, 0.25, -0.25)	6.27E-06	0.1591	0.0280	0.0723
(0, 0.25, -0.25)	5.22E-05	0.4925	0.0303	0.1319
(15.43, 0.25, -0.75)	5.92E-06	0.1710	0.0045	0.0182
(15.43, 0.25, -0.25)	5.09E-06	0.1560	0.0072	0.0331

Table 4
Turbulent Characteristics for Downward Flow with Insulating Walls.

(x/b, y/b, z/b)	TKE [m^2/s^2]	Turbulence Intensity x	Turbulence Intensity y	Turbulence Intensity z
(-15.43, 0.25, -0.75)	0.002335	3.3160	0.3439	0.7476
(-15.43, 0.25, -0.25)	0.001094	1.8125	0.2587	1.4559
(0, 0.25, -0.25)	0.0014	2.0423	0.1857	1.6723
(15.43, 0.25, -0.75)	0.000172	0.891	0.0383	0.2537
(15.43, 0.25, -0.25)	0.000182	0.7424	0.0217	0.5979

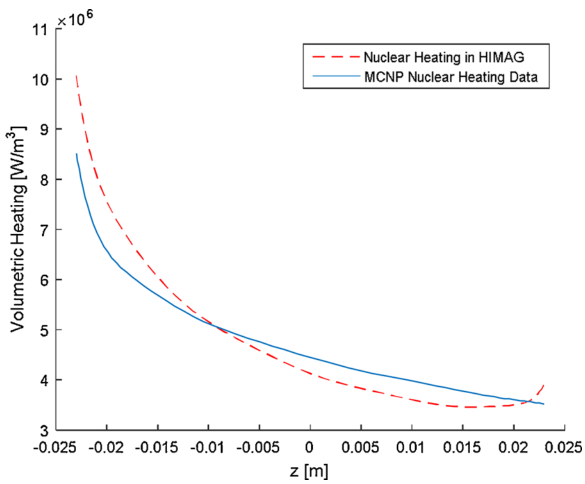

Fig. 23. Volumetric heating profiles. Both heating distributions have the same total heating per axial length Q' = 0.01 MW/m when integrated over the fluid cross-section. The heating is uniform along the y-direction.

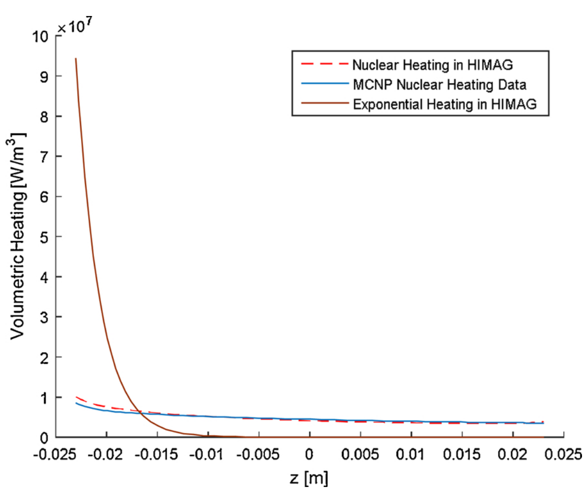

Fig. 24. Volumetric heating profiles. All three heating distributions have the same total heating per axial length Q' = 0.01 MW/m when integrated over the fluid cross-section. The heating is uniform along the y-direction.

the plasma can influence the heating curve in the breeding material. For the present analysis, a heating curve is constructed to resemble the heating produced in PbLi in a wedge piece of a 3D torus which represents a piece of tokamak simulated by Riva et al. (2017) [36] using MCNP6 1.0 neutron transport code with ENDFB/VII.0. The PbLi is situated behind a thin (5 mm) first wall composed of ferritic steel which bounds the plasma region in the center of the wedge. This configuration most closely corresponds to the heating inside a self-cooled blanket, though the volumetric heating inside the walls and the surface heating on the first wall by bremsstrahlung radiation are not included. In Fig. 23, the heating profile used in the present analysis is compared with the first 5 cm of the heating curve produced in MCNP for an outboard LM blanket with PbLi at the equator of a tokamak.

Here, the curves have been scaled such that their total heating per unit length is the same ($Q' = 0.01$ MW/m), assuming that the heating is uniform along the ydirection inside the fluid. In Fig. 23, the dashed red curve is given by the following polynomial and parameters as implemented in HIMAG:

$$q'''(z) = p1^*\left(\frac{z}{a}+1\right)^{10} + p2^*\left(\frac{z}{a}+1\right)^{9}\ldots$$
$$+ p3^*\left(\frac{z}{a}+1\right)^{8} + p4^*\left(\frac{z}{a}+1\right)^{7}\ldots$$
$$+ p5^*\left(\frac{z}{a}+1\right)^{6} + p6^*\left(\frac{z}{a}+1\right)^{5}\ldots$$
$$+ p7^*\left(\frac{z}{a}+1\right)^{4} + p8^*\left(\frac{z}{a}+1\right)^{3}\ldots$$
$$+ p9^*\left(\frac{z}{a}+1\right)^{2} + p10^*\left(\frac{z}{a}+1\right) + p11, \tag{16}$$

$a = 0.023$ m,

$C = 1.012055394224199\text{e}+07$ W/m^3,

$p1 = 0.017569865669577\text{e}2^*C$,

$p2 = -0.181685787408323\text{e}2^*C$,

$p3 = 0.808211328842193\text{e}2^*C$,

$p4 = -2.023006874524559\text{e}2^*C$,

$p5 = 3.130259698018951\text{e}2^*C$,

$p6 = -3.100016305296208\text{e}2^*C$,

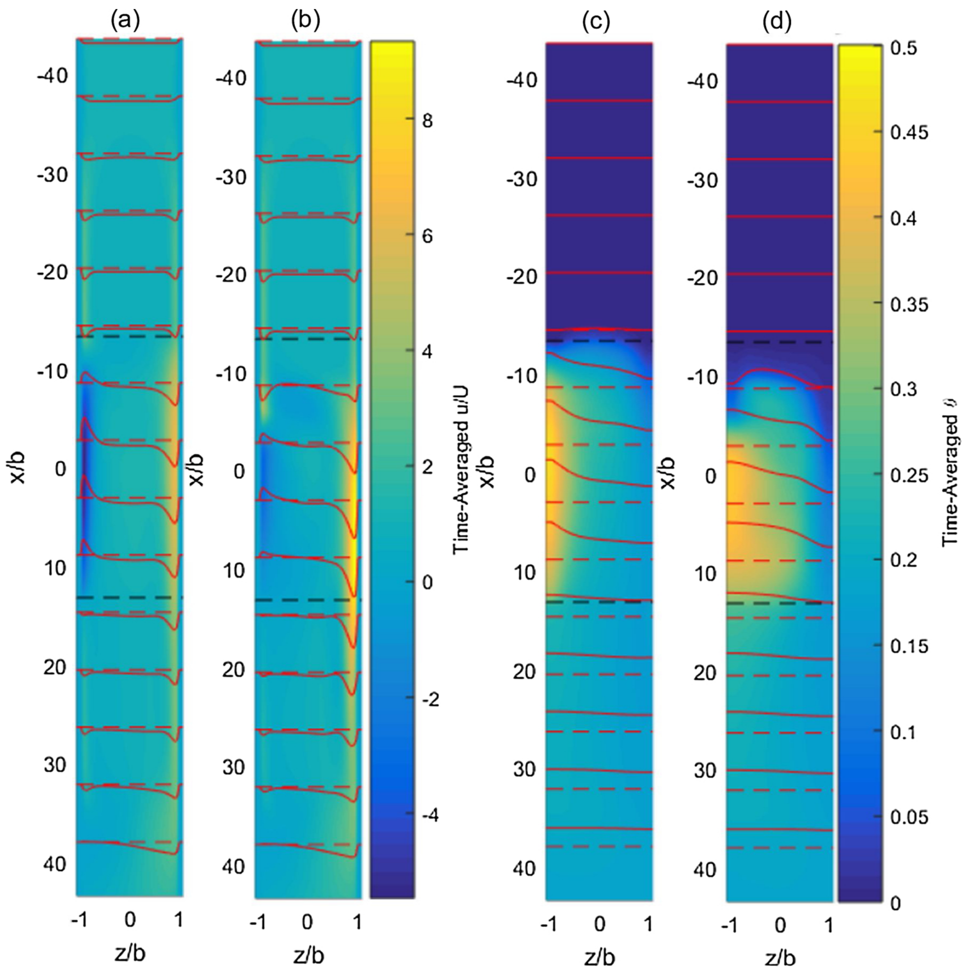

Fig. 25. (a,b) Time-averaged axial velocity and (c,d) time-averaged temperature on the y = 0 center-plane. Ha = 220, Re = 2027, Gr = 1.57×10^8, c_w = 0.12, downward flow with either (a,c) exponential heating, or (b,d) nuclear heating. The flow enters from the top in the direction of gravity. The z-axis is stretched compared to the x-axis by a factor of 5 to more easily view the entire flow field. The dashed, red lines spaced every 5.78 characteristic lengths are the zero lines for the profiles which are solid red lines. The dashed, black lines mark the bounds of the heated region (For interpretation of the references to colour in this figure legend, the reader is referred to the web version of this article.).

$p7 = 1.971743300940257e2*C$,

$p8 = -0.792480180180538e2*C$,

$p9 = 0.198526103983034e2*C$,

$p10 = -0.034988089715951e2*C$,

$p11 = 0.009946374499912e2*C$.

Here, C is the maximum heating, a is the duct half width, z = [0.023 m, 0.023 m], and q''' is given in W/m^3.

In the present analysis, the buoyant effects produced by the nuclear heating distribution given by Eq. (16) are compared with the buoyant effects produced by a much steeper heating profile that is constructed using an exponential formulation. The present analysis' exponential heating curve is plotted along with the nuclear heating curves in Fig. 24 below.

The curves shown in Fig. 24 all have the same total heating per unit length (Q' = 0.01 MW/m), assuming that the heating is uniform along the y-direction inside the fluid. The exponential heating curve above is given by:

$$q'''(z) = C^*exp\left(-M^*\left(\frac{z}{a} + 1\right)\right), \quad (17)$$

$M = 10$,

$C = 9.451795860691433e+07$ W/m^3,

$a = .023$ m.

Here, C is the maximum heating, a is the duct half width, z = [-0.023 m, 0.023 m], q''' is given in W/m^3, and M is the shape parameter which determines the steepness of the exponential curve. A shape parameter of $M = 1$ would more closely approximate the nuclear heating curves while the high value of $M = 10$ should yield buoyant effects similar to surface heating at the same Q'.

The volumetric heating in the present simulations is applied uniformly along the y-direction in the fluid domain only. The details of the volumetric heating have been given in dimensional form because HIMAG is a dimensional code. However, the presented results have been nondimensionalized by the characteristic values.

3.4.1. Comparison of downward flow with conducting walls

For downward flow in conducting ducts, the exponential heating case, on average, features a longer, thinner reverse flow bubble in the base flow compared to the nuclear heating case (Fig. 25), with the initial boundary layer separation occurring further upstream ($x/b \sim -8.7$ vs. $x/b \sim -4.3$) and the final boundary layer reattachment occurring further downstream ($x/b \sim 13$ vs. $x/b \sim 8.7$). Additionally, the base flow of the exponential heating case features faster reverse flow on the hot sidewall, but also slower forward flow near the cold sidewall and, in general, caries a higher flowrate in the bulk compared to the nuclear heating base flow. Due to the higher concentration of heating near the hot sidewall in the exponential heating case, the time-averaged temperature distribution includes generally steeper gradients and higher temperatures near the hot wall compared to the nuclear heating case but also has a flatter time-averaged z-direction temperature gradient near the cold wall and is generally colder in the bulk. Interestingly, due to the faster forward flow at the cold wall in the nuclear heating case, the temperature is colder there compared to the exponential case as the

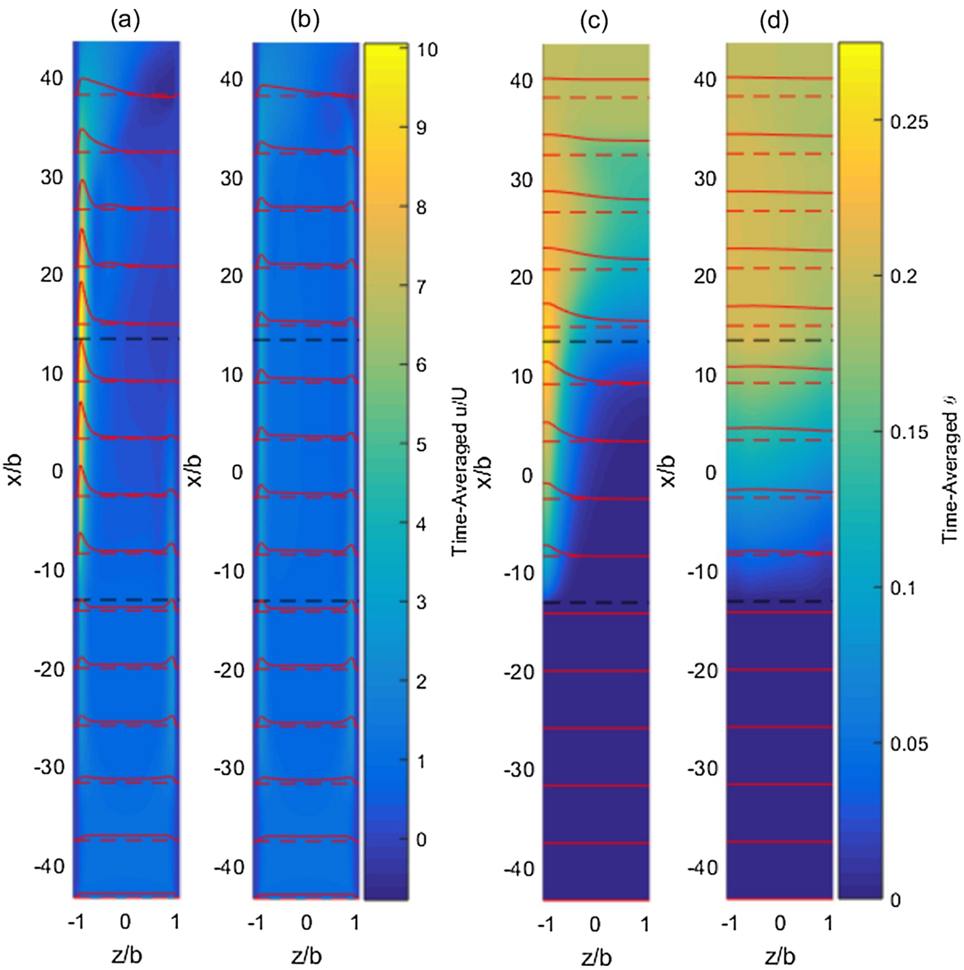

Fig. 26. (a,b) Time-averaged axial velocity and (c,d) time-averaged temperature on the y = 0 center-plane. Ha = 220, Re = 2027, Gr = 1.57×10^8, $c_w = 0.12$, upward flow with either (a,c) exponential heating, or (b,d) nuclear heating. The flow enters from the bottom opposite the direction of gravity. The z-axis is stretched compared to the x-axis by a factor of 5 to more easily view the entire flow field. The dashed, red lines spaced every 5.78 characteristic lengths are the zero lines for the profiles which are solid red lines. The dashed, black lines mark the bounds of the heated region (For interpretation of the references to colour in this figure legend, the reader is referred to the web version of this article.).

competition between advection and diffusion terms becomes more important than the volumetric heating term near the cold wall. The nuclear heating case features a unique behavior near the entrance to the heated region where the temperature maximum is in the center of the duct instead of near the hot wall for ~8.7 characteristic lengths until the location of boundary layer separation. In this region, the side layer jets from the M-shaped profile upstream are still strong enough to advect the heat downstream while the balance between conduction and the applied heating term dominates the temperature solution in the slower bulk flow.

3.4.2. Comparison of upward flow with conducting walls

For upward flow in conducting ducts, the buoyant effects are much stronger in the exponential heating case than in the nuclear heating case (Fig. 26). Firstly, there is significant flow asymmetry in the heated region of the exponential case with a large buoyant jet forming on the hot sidewall while the side layer jet on the cold wall shrinks to nothing near $x/b \sim 8.7$. In the nuclear heating case however, the flow remains M-shaped with much smaller velocity asymmetry in the z-direction and more flow carried in the bulk and in the cold side layer than the exponential heating flow. Both flows are stable. The temperature profiles show higher temperatures in the exponential case due to the heat being concentrated at the hot wall where advection associated with the large buoyant jet balances the volumetric heating term. As such, a thin thermal boundary layer exists in the heated region and the cold wall remains at the inlet temperature until the end of the heated region. The opposite is true in the nuclear heating case which features much flatter temperature and velocity profiles as the solution is dominated by the balance of conduction and the more evenly distributed volumetric heating term. Consequently, the temperature maximum is in the bulk rather than near the sidewall and there is only slight temperature asymmetry along the z-direction.

3.4.3. Comparison of downward flow with insulating walls

For downward flow in insulating ducts, both the exponential heating case and the nuclear heating case feature large scale flow instability in the heated region which is caused by buoyant effects via the axial temperature gradient as in Rayleigh-Taylor instability. In the time-averaged sense (Fig. 27), the exponential case has higher time-averaged temperatures and temperature gradients than the nuclear case near the hot wall. As the buoyant effects are therefore stronger, the exponential case features a longer and thicker reverse flow region attached to the hot wall with buoyant flow propagating upstream of the heated region by ~5.7 characteristic lengths while in the nuclear heating case, the reverse flow begins only after the beginning of the heated region. This is because the higher concentration of heating in the exponential case is sufficient for driving buoyant convection of hot fluid that propagates upstream until cooled enough by conduction to be swept downstream by the oncoming MHD flow. In the nuclear case, the buoyant recirculation of flow is limited to the heated region. Moreover, in the exponential heating case, the reverse flow and the forward flow demonstrate higher speed.

3.4.4. Comparison of upward flow with insulating walls

The nuclear heating flow has no thermal boundary layer and the temperature profile is nearly uniform though it is slightly asymmetric, accounting for the velocity asymmetry along the z-direction. Consequences of the high concentration of heating in the exponential

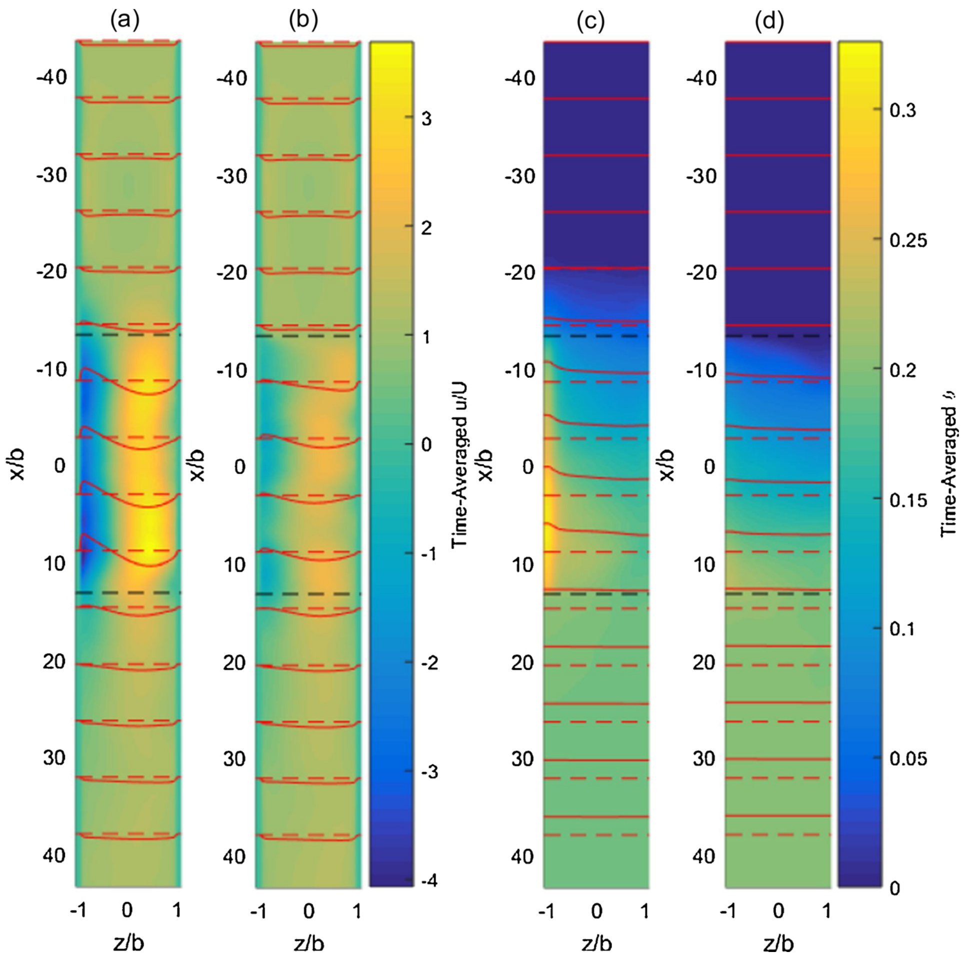

Fig. 27. (a,b) Time-averaged axial velocity and (c,d) time-averaged temperature on the y = 0 center-plane. Ha = 220, Re = 2027, Gr = 1.57×10^8, c_w = 0.12, downward flow with either (a,c) exponential heating, or (b,d) nuclear heating. The flow enters from the top in the direction of gravity. The z-axis is stretched compared to the x-axis by a factor of 5 to more easily view the entire flow field. The dashed, red lines spaced every 5.78 characteristic lengths are the zero lines for the profiles which are solid red lines. The dashed, black lines mark the bounds of the heated region (For interpretation of the references to colour in this figure legend, the reader is referred to the web version of this article.).

case include higher temperature and temperature gradient near the hot wall, and lower temperature away from the hot wall where the transverse temperature gradient is very flat. Furthermore, nearly 100 % of the flow rate is carried by the buoyant jet near the hot wall in the exponential heating case while the flow stagnates or recirculates weakly elsewhere. Meanwhile, some of the nuclear heating flow is still carried inside the bulk and the cold side layer (Fig. 28).

3.4.5. Comparison with surface heating scenarios

Now we go further to compare the results of the exponential heating and nuclear heating cases with the surface heating cases described in section 3.1 for the same $Re = 2027$, $Ha = 220$, and $Q' = 0.01$ MW/m ($Gr = 1.44 \times 10^8$) and including all four configurations of upward/downward and conducting/insulating ducts. Though the total heating is the same in all cases presented in Section 3.4, the characteristic temperatures are different for surface heating cases compared to volumetric heating cases. The difference is due to the surface being applied over $y = -b - t_w$ to $b + t_w$ while the volumetric heating is applied from $y = -b$ to $y = b$. This results in $q''_{surface}$ being 8% smaller than q''_{volume}. However, both cases are directly comparable since the total heating applied to the system is the same. Because nondimensionalizing by ΔT would scale the two cases differently by 8%, the following direct comparisons are made using the dimensional results for PbLi flowing with b = 0.023 m, U = 0.02 m/s, B = 0.5 T, and ΔT = 350.5 °C and 381 °C for surface and volumetric heating cases respectively. Time-averaged velocity and temperature profiles at x = 0 m, y = 0 m are plotted in Figs. 29 and 30.

As demonstrated in the figures above, the results of the exponential heating case are in close agreement with the surface heating case except for the downward insulating case which exhibits somewhat stronger buoyant effects in the surface heating case. The results of the nuclear heating cases then differ from the surface heating cases' results as they did from the exponential heating results in the above analysis. This follows from the concept that as the heating distribution becomes more concentrated near the hot wall, volumetric heating eventually becomes indistinguishable from surface heating. Inside the hot wall, the surface heating cases show much higher temperatures. This is merely a consequence of the boundary conditions and has not been shown to have a significant effect on the flow.

Despite significant differences between results, many of the same phenomena occur for both nuclear heating and the steeper exponential heating cases. For instance, reverse flow occurs in all the downward flows studied here, though the values and magnitude of the velocity and temperature fluctuations were found to depend on the heating distribution. Additionally, velocity asymmetry occurs in all the upward cases, though again, the magnitude of this effect at constant Q' is also dependent on the heating distribution.

Though surface heating is more attainable in laboratory settings, future numerical efforts should consider using nuclear heating distributions at higher Gr to more closely model fusion reactor conditions. Since the nuclear heating case exhibits weaker buoyant effects than the surface heating case with the same Q', perhaps the flow behavior of surface heating cases better approximates nuclear heating cases with much higher Q'. Consider that increasing Q' by scaling up the magnitude of the nuclear heating will also increase the gradient of the heating by a proportional amount. Thus, it follows that the temperature gradients will be steeper and the buoyant effects will be stronger.

The differences between upward and downward flows or differences between conducting and insulating ducts are associated with significant differences in the types of phenomena observed while the differences caused by varying the heating profiles were more a matter of magnitude

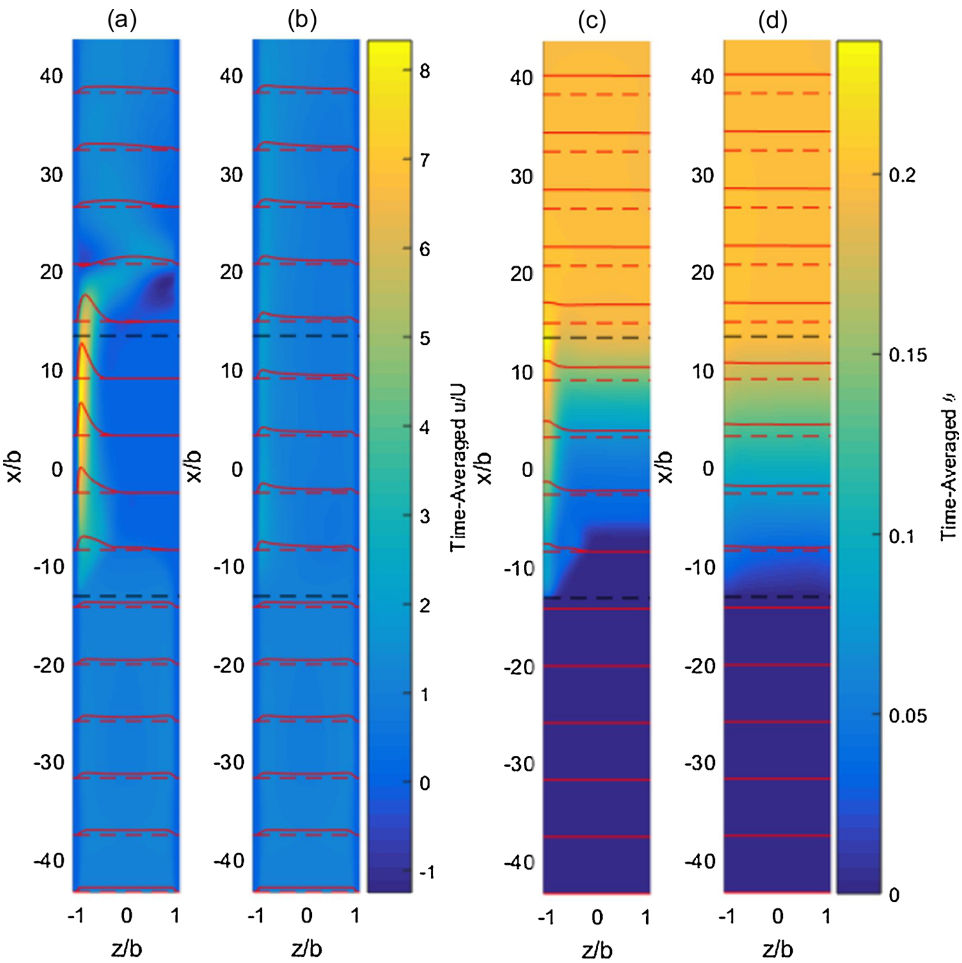

Fig. 28. (a,b) Time-averaged axial velocity and (c,d) time-averaged temperature on the y = 0 center-plane. Ha = 220, Re = 2027, Gr = 1.57 × 10^8, c_w = 0.12, upward flow with either (a,c) exponential heating, or (b,d) nuclear heating. The flow enters from the bottom opposite the direction of gravity. The z-axis is stretched compared to the x-axis by a factor of 5 to more easily view the entire flow field. The dashed, red lines spaced every 5.78 characteristic lengths are the zero lines for the profiles which are solid red lines. The dashed, black lines mark the bounds of the heated region (For interpretation of the references to colour in this figure legend, the reader is referred to the web version of this article.).

such that surface heating has been proven to serve as a reasonable approximation for the volumetric heating profile in experimental settings; however, it can be expected that surface heating cases will have somewhat stronger buoyant effects than volumetric heating cases with the same *Q'*. Surface heating cases can be simulated using either purely surface heating (i.e. through the boundary conditions) or exponential volumetric heating at high *M* (i.e. through the source term on the RHS of the energy equation). These conclusions were made by comparing instantaneous and time-averaged temperature and velocity fields.

4. Conclusions

HIMAG was used to simulate the 3D flow of liquid metal through vertical, square ducts to explore the MHD mixed convection phenomena which may occur in breeder blankets of fusion power reactors. A fringing, transverse magnetic field provided a region of uniform field which was centered on a region of applied, one-sided heating that the pressure driven liquid metal was made to flow through.

MHD mixed convection phenomena were described in an overview of the flow behavior at $Ha = 220$, $Re = 2027$, and $Gr = 1.44 \times 10^8$ for the case of applied surface heating at a sidewall. The flow orientation was varied (upward/downward) and the electrical conductivity of the duct walls was varied ($c_w \sim 0$ or 0.12) to provide four scenarios to study. The upward, buoyancy assisted flows in the overview featured relatively stable flows with strong jets attached to the hot wall and almost no flow carried by the bulk. The downward, buoyancy opposed flows featured flow reversal, higher temperatures, and flow instability in the heated region.

A study on the effect of *Ha*, *Re*, and *Gr* was performed for upwards and downwards flows in conducting ducts with applied surface heating for *Ha* ranging from 110 to 880, *Re* from 2027 to 20,270, and two choices of $Gr = 1.44 \times 10^8$, 3.6×10^8. As expected, increasing *Re* decreased buoyant effects, going as far as to change the flow regime from that of MHD mixed convection ($Re = 2027$) to that of MHD forced flow ($Re \geq 15{,}201$). Predictably, increasing *Gr* increased buoyant effects while increasing *Ha* had a more subtle influence on buoyant effects: increasing *Ha* reduced the reverse flow velocity near the hot sidewall while also causing the temperature there to increase due to improved stability and thus reduced advection heat transfer normal to the wall.

A novel metric for evaluating the velocity nonuniformity along the magnetic field direction was presented and applied to four flow scenarios with either upward or downward flow through conducting or insulating ducts with applied surface heating on one sidewall ($Ha = 220$, $Re = 2027$, and $Gr = 1.44 \times 10^8$). The metric, along with plots of kinetic energy, was useful in investigating the flow's departure from quasi-2D behavior in particular circumstances. The analysis yielded 3 major conclusions:

(1) In downward flow cases, feedback between the temperature and the velocity fields promoted lasting asymmetry in both fields along the magnetic field direction. It was found that the temperature of the Hartmann walls would differ, in the time-averaged sense, by $\Delta\theta \sim 0.17$ in conducting downward flow. In upward flows, this feedback mechanism promotes uniformity along the magnetic field direction instead. Interestingly, such asymmetry was not observed in cases with relatively weaker buoyancy effects as in the case of downward flow in a conducting duct at $Ha = 220$, $Re = 3041$, $Gr = 2.88 \times 10^7$ [27]. This implies that a stability threshold exists for this effect, one that is likely characterized by the competition of buoyant effects with stabilizing electromagnetic effects and diffusion.

(2) Buoyancy reduces the velocity uniformity along the magnetic

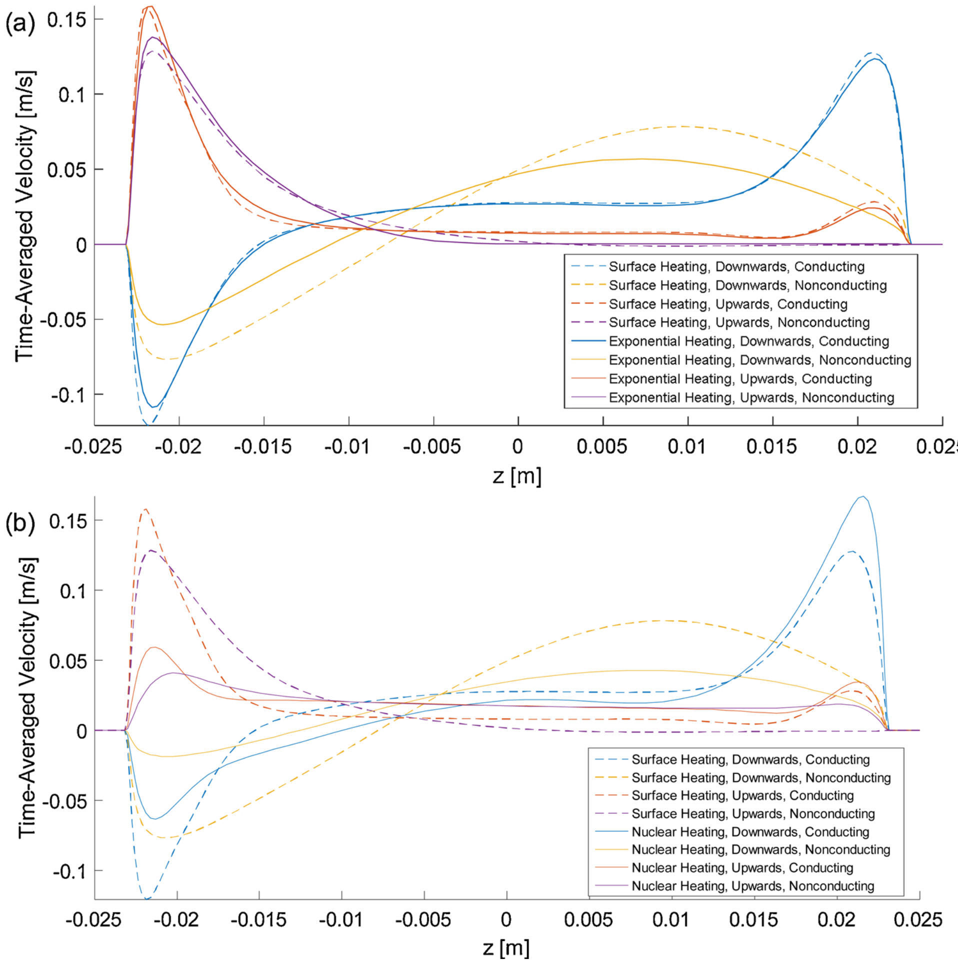

Fig. 29. A comparison of time-averaged velocity profiles at x = y = 0 m for flows with (a) exponential volumetric heating and (b) nuclear volumetric heating in the fluid domain or surface heating applied to the outside surface of the duct wall at $z = -t_w$-a. In all cases, the total heating is the same. Ha = 220, Re = 2027, c_w = 0.12 or ~0, Gr = 1.57×10^8 for volumetric heating scenarios and Gr = 1.44×10^8 for surface heating scenarios.

field direction by promoting inertial transfers of momentum. This effect is strongest in downward flows where boundary layer separation occurs. In the cases presented, the boundary layer separation cooccurs with the location of maximum kinetic energy and maximum y-non-uniformity of the flow.

(3) While the buoyant force diminishes uniformity along the magnetic field direction, Joule dissipation is still present, and the resulting behavior of the combined effects is a turbulent flow which has velocity fluctuations in 3D, though the fluctuations parallel to the magnetic field are ~1 order of magnitude smaller, in terms of kinetic energy and turbulence intensity, than fluctuations which are perpendicular to the magnetic field.

Eight cases consisting of two types of volumetric heating curves (nuclear heating given by a neutronics code or an exponential heating curve which is somewhat steeper but has the same total heating) for each of four flow scenarios with different combinations of flow orientation (up/down) and wall conductivity ($c_w = 0.12$ or ~ 0) were simulated to explore the effect of varying the volumetric heating distribution in MHD mixed convection flows. Despite having the same dimensionless parameters ($Ha = 220$, $Re = 2027$, $Gr = 1.57 \times 10^8$), the steeper exponential heating case featured markedly stronger buoyant effects compared to the nuclear heating case in all four scenarios due to higher concentration of heating near the hot wall. However, the same kinds of phenomena were observed in cases with the same flow orientation and wall conductivity despite differences in heating. This observation also applies to the comparison with surface heating cases of the same total heating, Ha, Re, c_w, and flow orientation, justifying the use of surface heating as a suitable substitute for volumetric nuclear heating in experiments that aim to explore the MHD mixed convection phenomena in flows with steep gradients in volumetric heating. This is a useful conclusion since volumetric heating cannot implemented in laboratory experiments.

CRediT authorship contribution statement

Tyler J. Rhodes: Conceptualization, Methodology, Software, Formal analysis, Investigation, Resources, Data curation, Writing - original draft, Writing - review & editing, Visualization. **Gautam Pulugundla:** Conceptualization, Methodology, Investigation, Resources, Data curation, Writing - review & editing, Visualization. **Sergey Smolentsev:** Conceptualization, Methodology, Resources, Writing - review & editing, Supervision. **Mohamed Abdou:** Conceptualization, Resources, Writing - review & editing, Supervision, Project administration, Funding acquisition.

Declaration of Competing Interest

The authors declare that they have no known competing financial interests or personal relationships that could have appeared to influence the work reported in this paper.

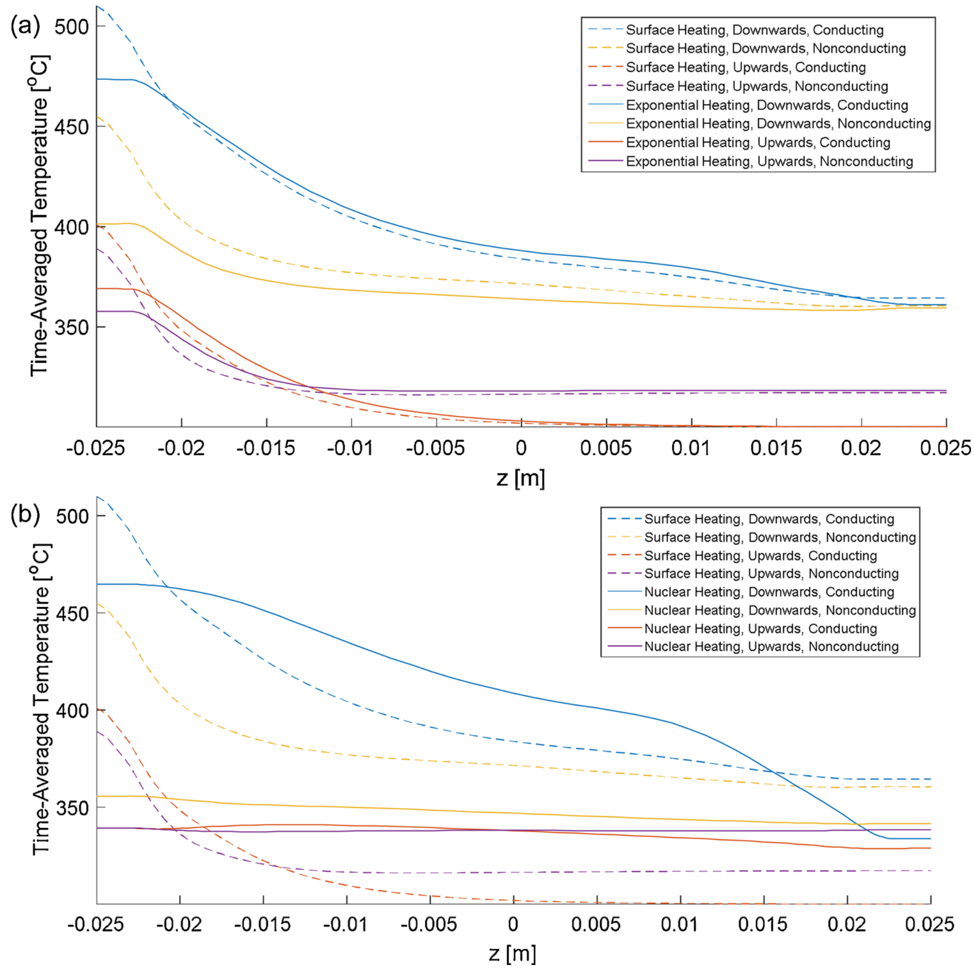

Fig. 30. A comparison of time-averaged temperature profiles at $x = y = 0$ m for flows with (a) exponential volumetric heating and (b) nuclear volumetric heating in the fluid domain or surface heating applied to the outside surface of the duct wall at $z = -t_w - a$. In all cases, the total heating is the same. Ha = 220, Re = 2027, $c_w = 0.12$ or ~ 0, Gr = 1.57×10^8 for volumetric heating scenarios and Gr = 1.44×10^8 for surface heating scenarios.

Acknowledgements

This paper is based on the dissertation of Tyler Rhodes. This work was performed with support from US Department of Energy, Office of Fusion Energy Sciences, under Grant No. DE-FG02-86ER52123. The numerical efforts of this research used resources of the National Energy Research Scientific Computing Center (NERSC), a U.S. Department of Energy Office of Science User Facility operated under Contract No. DE-AC02-05CH11231.

References

[1] M. Sawan, E. Marriott, M. Dagher, Neutronics performance parameters for the US dual coolant lead lithium ITER test blanket module, 2009 23rd IEEE/NPSS Symposium on Fusion Engineering, IEEE, 2009.
[2] M. Abdou, N.B. Morley, S. Smolentsev, A. Ying, S. Malang, A. Rowcliffe, M. Ulrickson, Blanket/first wall challenges and required R&D on the pathway to DEMO, Fusion Eng. Des 100 (2015) 2–43.
[3] L. Bühler, Laminar buoyant magnetohydrodynamic flow in vertical rectangular ducts, Phys. Fluids 10 (1998) 223–236.
[4] C. Mistrangelo, L. Bühler, Numerical analysis of buoyant-convective liquid metal flow in channels exposed to strong magnetic fields, 2011 IEEE/NPSS 24th Symposium on Fusion Engineering, IEEE, 2011.
[5] O. Zikanov, A. Thess, J. Sommeria, Turbulent Convection Driven by an Imposed Temperature Gradient in the Presence of a Constant Vertical Magnetic Field, Numerical Flow Simulation I, Springer, Berlin, Heidelberg, 1998, pp. 187–199.
[6] I. Melnikov, N. Rasuvanov, V. Sviridov, E. Sviridov, A. Shestakov, An investigation of heat exchange of liquid metal during flow in a vertical tube with non-uniform heating in the transverse magnetic field, Therm. Eng. 60.5 (2013) 355–362.
[7] I. Kirillov, D. Obukhov, L. Genin, V. Sviridov, N. Razuvanov, V. Batenin, I. Belyaev, I. Poddubnyi, N. Pyatnitskaya, Buoyancy effects in vertical rectangular duct with coplanar magnetic field and single sided heat load, Fusion Eng. Des. 104 (2016) 1–8.
[8] I. Belyaev, P. Frick, N. Razuvanov, E. Sviridov, V. Sviridov, Temperature fluctuations in a nonisothermal mercury pipe flow affected by a strong transverse magnetic field, Int. J. Heat Mass Transf. 127 (2018) 566–572.
[9] S. Smolentsev, R. Moreau, M. Abdou, Characterization of key magnetohydrodynamic phenomena for PbLi flows for the US DCLL blanket, Fus. Eng. Des. 83 (2008) 771–783.
[10] G. Sposito, M. Ciofalo, Fully developed mixed magnetohydrodynamic convection in a vertical square duct, Numer. Heat Transf. Part A Appl. 53.9 (2008) 907–924.
[11] H. Saleh, I. Hashim, Flow reversal of fully-developed mixed MHD convection in vertical channels, Chinese Phys. Lett. 27.2 (2010) 024401.
[12] C. Mistrangelo, L. Bühler, Numerical study of fundamental magnetoconvection phenomena in conducting ducts, IEEE Trans. Plasma Sci. 40.3 (2012) 584–589.
[13] M. Chutia, P. Deka, Numerical study on MHD mixed convection flow in a vertical insulated square duct with strong transverse magnetic field, J. Appl. Fluid Mech. 8.3 (2015).
[14] X. Zhang, O. Zikanov, Two-dimensional turbulent convection in a toroidal duct of a liquid metal blanket of a fusion reactor, J. Fluid Mech. 779 (2015) 36–52.
[15] X. Zhang, O. Zikanov, Mixed convection in a downward flow in a vertical duct with strong transverse magnetic field, arXiv preprint (2018) arXiv:1804.02659.
[16] L. Liu, O. Zikanov, Elevator mode convection in flows with strong magnetic fields, Phys. Fluids 27.4 (2015) 044103.
[17] N. Vetcha, Study of Instability and Transition in MHD Flows As Applied to Liquid Metal Blankets, Diss. UCLA, 2012.
[18] N. Vetcha, S. Smolentsev, M. Abdou, R. Moreau, Study of instabilities and quasi-two-dimensional turbulence in volumetrically heated MHD flows in a vertical rectangular duct, Phys. Fluids 25 (2013) 024102.
[19] O. Zikanov, Y. Listratov, Numerical investigation of MHD heat transfer in a vertical round tube affected by transverse magnetic field, Fusion Eng. Des. 113 (2016) 151–161.
[20] Y. Listratov, D. Ognerubov, O. Zikanov, V. Sviridov, Numerical simulations of mixed convection in liquid metal flow within a horizontal pipe with transverse magnetic field, Fluid Dyn. Res. 50.5 (2018) 051407.
[21] R. Munipalli, S. Shankar, M. Ni, N. Morley, Development of a 3D Incompressible

Free Surface MHD Computational Environment for Arbitrary Geometries: HIMAG, DOE SBIR Phase-II Final Report, (2003).
[22] S. Smolentsev, R. Moreau, L. Buhler, C. Mistrangelo, MHD thermofluid issues of liquid-metal blankets: phenomena and advances, Fusion Eng. Des. 85 (2010) 1196–1205.
[23] P. Crapper, W. Baines, Non boussinesq forced plumes, Atmos. Environ. 11.5 (1977) 415–420.
[24] D. Gray, A. Giorgini, The validity of the Boussinesq approximation for liquids and gases, Intl. J. Heat Mass Transfer 19 (1976) 545–551.
[25] P.-E. Roche, Applicability of Boussinesq approximation in a turbulent fluid with constant properties, arXiv preprint (2007) arXiv:0710.3497.
[26] M. Kiyoshi, Rational Derivation of the Boussinesq Approximation, (2019).
[27] M. De Les Valls, L. Sedano, L. Batet, I. Ricapito, A. Aiello, O. Gastaldi, F. Gabriel, Lead–lithium eutectic material database for nuclear fusion technology, J. Nucl. Mater. 376.3 (2008) 353–357.
[28] T. Rhodes, Numerical Study of 3D Magnetohydrodynamic Flows Towards Liquid Metal Blankets, Including Complex Geometry and Buoyancy Effects, Diss. UCLA, 2019.
[29] C. Pant, A. Bhattacharya, A viscous sponge layer formulation for robust large eddy simulation of thermal plumes, Comput. Fluids 134 (2016) 177–189.
[30] R. Holroyd, J. Walker, A theoretical study of the effects of wall conductivity, non-uniform magnetic fields and variable-area ducts on liquid-metal flows at high Hartmann number, J. Fluid Mech. 84.3 (1978) 471–495.
[31] L. Kit, D. Peterson, I. Platniek, A. Tsinober, Magnitn, Gidrodinam 4 (1970) 47.
[32] Tao Zhou, H. Chen, Z. Yang, Effect of fringing magnetic field on magnetohydrodynamic flow in rectangular duct, Fusion Eng. Des. 86.9 (2011) 2352–2357.
[33] J. Shercliff, Steady motion of conducting fluids in pipes under transverse magnetic fields, Math. Proc. Cambridge Philos. Soc. 49 (1953) 136–144.
[34] J. Hunt, Magnetohydrodynamic flow in rectangular ducts, J. Fluid Mech. 21.04 (1965) 577–590.
[35] J. Sommeria, R. Moreau, Why, How and When MHD turbulence becomes two dimensional? J. Fluid Mech. 118 (1982) 507.
[36] M. Riva, C. Di Sanzo, M. Abdou, M. Youssef, Reducing the Peak-to-Average-Power-Ratio in fusion blankets, Fus. Sci. Tech. 72.3 (2017) 469–477.